npj | clean water

Article

Published in partnership with King Fahd University of Petroleum & Minerals

https://doi.org/10.1038/s41545-025-00470-6

Analysis of microstructure properties of Ni-Fe MOFs and their influence on selective recognition of single and binary dye systems

Dan Xu[1,2,3,5], Xiaolin Cao[2,5], Jie Zhou[1,5], Zhihao Lin[1], Jing Wang[4] ✉, Jiatong Han[1], Ge Chen[1], Guangyang Liu[1,3] ✉, Xiaomin Xu[1], Yanguo Zhang[1] & Donghui Xu[1] ✉

To address the environmental threats posed by dye pollution, it is crucial to develop adsorbents with high selectivity and adsorption capacity for the removal of chemical dye pollutants. In this study, five types of Ni/Fe-MOFs were synthesized via a one-pot solvothermal method by varying the Ni/Fe molar ratio. Their physicochemical structures, surface morphologies, and compositions were characterized through a series of techniques, and their adsorption performances for different dyes were preliminarily investigated. The results demonstrated that the Ni/Fe ratio significantly affects the microstructure and adsorption performance of the MOFs. As the molar ratio of Ni/Fe increased, the structures of the five materials transformed from nanoflowers$_{(Fe\text{-}MOFs)}$ to nanospheres$_{(Ni/Fe(3:1)MOFs)}$, and eventually to rhombic blocks$_{(Ni\text{-}MOFs)}$. The specific surface area decreased from 281.3 $m^2/g_{(Fe\text{-}MOFs)}$ to 67.11 $m^2/g_{(Ni/Fe(1:1)MOFs)}$ and further to 0.5369 $m^2/g_{(Ni\text{-}MOFs)}$. XPS analysis confirmed the synergistic coordination between Ni and Fe, and FT-IR spectra revealed characteristic peaks for hydroxyl groups on the MOF surface and carboxylate ligands. XRD analysis indicated that materials with higher Ni content were more prone to ligand decomposition, which is consistent with the weight loss observed in the TG-DSC between 230 and 350 °C. The materials exhibited selective adsorption for different dyes. Under optimal conditions, the maximum adsorption capacities for Eosin Y (EY), Neutral Red (NR), and Acid Fuchsin (AF) were 54.92 $mg/g_{(Fe\text{-}MOFs)}$, 636.31 $mg/g_{(Ni\text{-}MOFs)}$, and 79.30 $mg/g_{(Ni/Fe(1:1)MOFs)}$, respectively. The adsorption kinetics followed a pseudo-second-order model, and the adsorption isotherms conformed to the Langmuir model, while Fe-MOFs and Ni/Fe(1:1) MOFs also exhibited compatibility with the Freundlich model. The adsorption mechanism primarily involved monolayer adsorption as the dominant process, with localized multilayer adsorption, as well as chemisorption, hydrogen bonding, hydroxyl interactions, and electrostatic interactions. These MOFs demonstrated high dye removal efficiency in actual water samples and fruit and vegetable juices, exhibiting excellent reusability and anti-interference capabilities. Importantly, compared with the single system, Fe-MOFs and Ni/Fe(1:1)MOFs exhibit competitive adsorption, and Ni-MOFs exhibit synergistic adsorption in the binary system. This study confirms that by adjusting the Ni/Fe molar ratio, MOFs with high selectivity and adsorption performance for different dyes can be designed, providing new theoretical insights and technical support for environmental remediation and food safety applications.

Organic dyes, widely utilized in textiles[1], printing[2], and dyeing[3], play a significant role in industrial production but also pose notable environmental and health risks. The extensive discharge of industrial organic dye wastewater into the environment primarily contaminates human health and the safety of aquatic flora and fauna through food and water sources[4,5]. Environmentally, the release of organic dyes into water bodies leads to water pollution and a decrease in dissolved oxygen levels, directly threatening the survival and reproduction of aquatic organisms. These dyes can also infiltrate soil via water, being absorbed by plants and potentially accumulating in higher organisms within the food chain, thus polluting the ecosystem[6,7].

A full list of affiliations appears at the end of the paper. ✉e-mail: w_jing2001@126.com; liuguangyang@caas.cn; xudonghui@caas.cn

From a food safety perspective, residues of organic dyes and their degradation products may enter the human body through the food chain, posing potential health threats. Upon exposure, organic dyes may harm the skin, respiratory tract, and other organs, potentially leading to chronic toxicity or carcinogenic effects[8,9]. Therefore, researching efficient and eco-friendly dye treatment technologies is of paramount importance for environmental protection and food safety.

Currently, the commonly employed technologies for the removal of organic dyes from wastewater primarily include physical methods (adsorption[10], membrane separation[11], magnetic separation[12]), chemical methods (advanced oxidation[13], chemical precipitation[14], electrochemical oxidation[15]), and biological methods (aerobic[16] and anaerobic[17] biological treatments). Among these, adsorption is considered an effective technique for removing organic dye pollutants due to its simplicity, low cost, and ease of subsequent collection and treatment. Common adsorbent materials such as activated carbon[18], silica gel[19], and iron oxide[20] are widely used in the adsorption studies of organic dyes. However, these traditional adsorbents often exhibit limitations in selectivity, reproducibility, and adsorption capacity. In recent years, metal-organic frameworks (MOFs) have emerged as highly promising novel adsorbents due to their highly ordered pore structures, tunable pore sizes, and high specific surface areas[21].

MOFs, characterized by their porous structures and tunability, are materials formed through the self-assembly of metal nodes and organic ligands. Their structure and functionality can be modulated by selecting different metals and ligands, showcasing extensive application potential in adsorption, catalysis, drug delivery, and other fields[22]. Bimetallic MOFs, composed of two distinct metals, further enhance structural diversity and functional properties[23]. Previous studies have reported on the adsorption and removal capabilities of bimetallic MOFs for various pollutants. For instance, Yu et al.[24] investigated a novel thiol-functionalized bimetallic Zn/Ni-MOF for the adsorption of Hg(II) from wastewater, achieving a maximum adsorption capacity of 744.4 mg/g, significantly surpassing the 328.8 mg/g of the monometallic Ni-MOF. Li et al.[25] explored the removal of bisphenol A (BPA) from water using a bimetallic Ti-In-MOF, demonstrating a 38% improvement in adsorption performance for 50 mg/L BPA compared to monometallic In/Ti-MOFs. Zhao et al.[26] examined the adsorption and removal of Cr(VI) from wastewater using a bimetallic Fe/Zr-MOF, finding that the Fe/Zr-MOFs exhibited significantly higher removal efficiency than pure Fe-MOFs. These studies indicate that bimetallic MOFs exhibit superior adsorption performance in complex environments compared to monometallic MOFs, underscoring their substantial potential for practical applications.

Among the various bimetallic combinations, selecting Ni and Fe to construct Ni-Fe MOFs offers several notable advantages. Firstly, both Ni and Fe are transition metals with rich coordination chemistry, enabling the formation of stable MOF structures[27,28]. Secondly, Ni^{2+} and Fe^{2+} possess unique chemical and physical properties. Nickel ions (Ni^{2+}) exhibit high catalytic activity and stability, excelling in molecular sieving and adsorption[29], while ferrous ions (Fe^{2+}) have strong redox activity[30]. The synergistic effect of these two metals can significantly enhance the overall performance of MOFs, such as increasing the number of active sites[31] and improving thermal and chemical stability[32]. Additionally, Ni-Fe MOFs, due to their highly ordered pore structure and tunable pore size, offer greater advantages in molecular recognition and selective adsorption[33].

It is noteworthy that by regulating the ratio of metal ions within MOFs, their microstructure and adsorption performance can be significantly influenced, enabling the selective adsorption of specific dyes[34,35]. Although various studies have reported the adsorption performance of different MOFs for single dyes, systematic research on the selective adsorption behavior and mechanisms of MOFs for multiple dyes in complex environments remains limited. Understanding these mechanisms is crucial for designing adsorbents with high efficiency and selectivity.

In this study, we synthesized five Ni/Fe MOFs materials using a one-pot solvothermal method based on Ni/Fe bimetals with different molar ratios. We characterized their physicochemical structures, surface morphologies, and compositions through a series of techniques, and preliminarily investigated their adsorption performance for various dyes. Based on the characterization and adsorption data, we initially screened the most promising materials for further study on their dye adsorption capabilities. Firstly, single-factor optimization experiments were conducted, including parameters such as adsorbent dosage, adsorption time, initial dye concentration, pH, and salt concentration. Binary adsorption experiments were performed to examine the effects of different dye components on adsorption performance and their competitive interactions. Additionally, the regeneration and reuse capabilities of the adsorbents were evaluated, and their application in real samples and the adsorption mechanisms were investigated. Our findings will provide theoretical support and technical guidance for the design of MOFs with high selectivity and adsorption performance, offering new insights for applications in environmental remediation and food safety.

Results

Characterization

The morphology and structure of the synthesized materials were initially examined using scanning electron microscopy (SEM), as illustrated in Fig. 1. Figure 1a–e depict SEM images of Ni-MOFs, Ni/Fe (1:1) MOFs, Fe-MOFs, Ni/Fe (3:1) MOFs and Ni/Fe (1:3) MOFs, respectively. As illustrated by the images, Ni-MOFs exhibit a smooth rhombohedral block structure, Fe-MOFs exhibit a nanoflower structure, and both Ni/Fe (1:3) MOFs and Ni/Fe (1:1) MOFs also exhibit nanoflower structures. Ni/Fe (3:1) MOFs exhibit a nanosphere structure. The compactness of the nanoflower structures varies, indicating that the Ni/Fe ratio significantly influences the microstructure of the MOFs. In Ni/Fe MOFs, as the molar ratio of Ni/Fe increases, the nanostructures become more compact; conversely, they become looser with a decreasing Ni/Fe ratio. These results also confirm the successful incorporation of Ni and Fe bimetals in the synthesis and structural regulation of MOFs materials.

Fourier-transform infrared spectroscopy (FT-IR) was employed to characterize the functional groups and chemical bonds of the materials, as depicted in Fig. 2a. Similar characteristic absorption peaks are evident among the materials. Peaks at 3429, 1618, and 1381 cm^{-1} are observed in all materials, corresponding to O–H bonds, C=C bonds, and methyl groups, indicating the involvement of N,N-dimethylacetamide in the material synthesis. Additionally, absorption peaks at 540 and 715 cm^{-1} are attributed to stretching vibrations of Fe–O/Ni–O bonds and the presence of Fe_2Ni (μ3-O) clusters[36,37]. These results demonstrate the successful participation of Ni and Fe in the preparation of MOFs materials.

The X-ray diffraction (XRD) patterns of the materials are shown in Fig. 2b. The peak around 22° in the XRD spectra is attributed to characteristic peaks of amorphous C–N compounds[38,39], resulting from partial decomposition of organic ligands. This peak is predominantly observed in the spectra of Ni-MOFs and Ni/Fe (3:1) MOFs with higher Ni content, whereas it is absent in the spectra of Fe-MOFs, Ni/Fe (1:3) MOFs, and Ni/Fe (1:1) MOFs with higher Fe content. This observation suggests that MOFs with higher Fe content are less prone to decomposition compared to those with higher Ni content, indicating superior thermal stability.

To further investigate the thermal stability of the synthesized materials, thermogravimetric analysis coupled with differential scanning calorimetry (TG-DSC) was performed. The specific weight-loss data for each stage can be found in Supplementary Table 1. As depicted in Fig. 2c, the first weight-loss step (below 230 °C) is attributed to the loss of absorbed water and crystalline water from the samples. Between 230 and 350 °C, the second weight-loss step occurs due to decomposition of the MOFs precursors. Upon further heating above 350 °C, a third weight-loss step is observed, indicating the release of gaseous by-products such as CO_2, CO, N_2, and H_2O from the decomposition of large organic ligands, leading to the formation of porous structures rich in porous NiO and $NiFe_2O_4$ phases[40,41].

From the TG-DSC analysis, it is evident that MOFs with higher Ni content, such as Ni-MOFs and Ni/Fe (3:1) MOFs, undergo three weight-loss

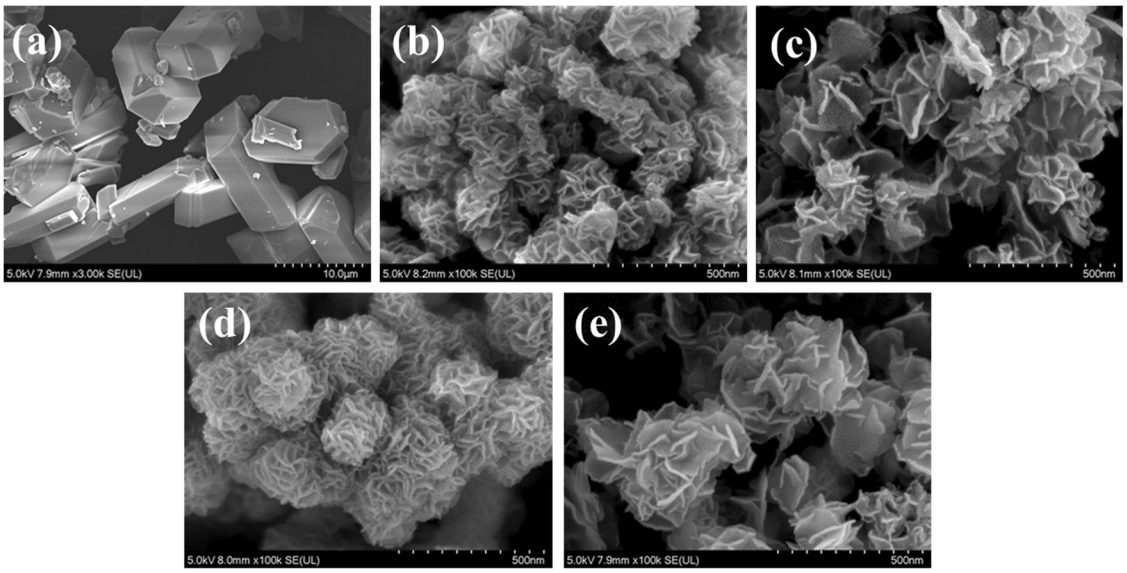

Fig. 1 | SEM images of Ni/Fe-MOFs with varying Ni/Fe ratios. Scanning electron microscopy (SEM) images of synthesized MOFs: **a** Ni-MOFs exhibit smooth rhombic blocks; **b** Ni/Fe (1:1) MOFs display nanoflower structures with intermediate compactness; **c** Fe-MOFs show loosely packed nanoflowers; **d** Ni/Fe (3:1) MOFs feature nanospheres; **e** Ni/Fe (1:3) MOFs retain nanoflower morphology but with reduced density. Structural transitions from nanoflowers to nanospheres and rhombic blocks correlate with increasing Ni/Fe ratios, confirming the tunability of MOF microstructures.

Fig. 2 | Structural and compositional characterization of Ni/Fe-MOFs. a FT-IR spectra showing O–H (3429 cm^{-1}), C=C (1618 cm^{-1}), and Fe/Ni–O (540–715 cm^{-1}) bonds. **b** XRD patterns highlighting amorphous C–N peaks (22°) in Ni-rich MOFs. **c** TG-DSC curves demonstrating thermal stability: Ni-MOFs undergo three weight-loss steps (water loss, precursor decomposition, and organic ligand degradation), while Fe-rich MOFs show two steps. **d** XPS full spectra confirming the presence of Fe, Ni, C, N, and O.

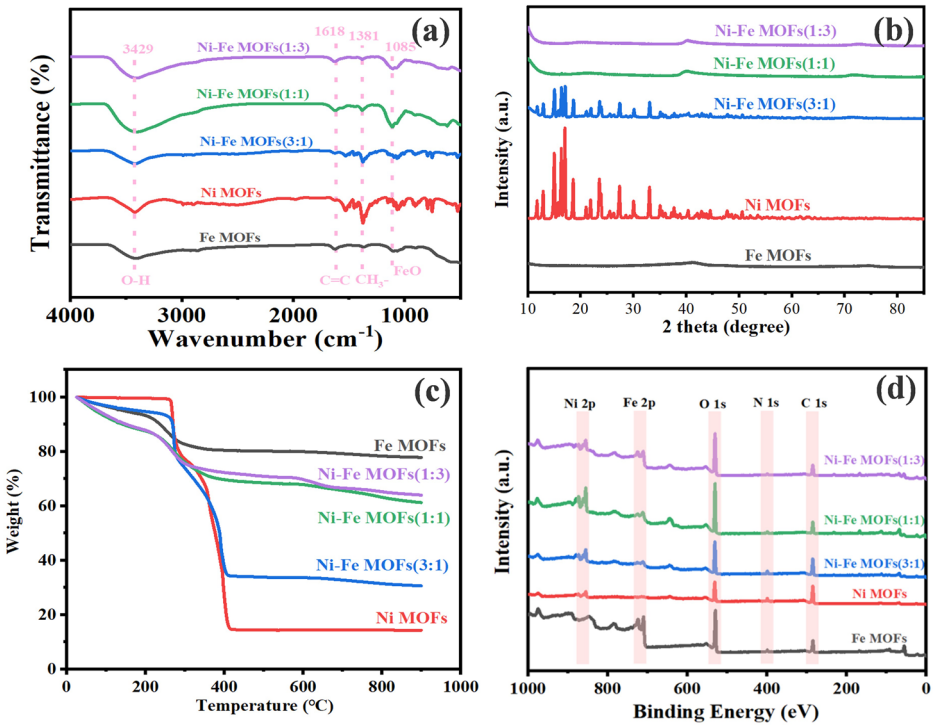

steps, whereas MOFs with higher Fe content, including Fe-MOFs, Ni/Fe (1:3) MOFs, and Ni/Fe (1:1) MOFs, primarily exhibit two weight-loss steps. This observation indicates that MOFs with higher Fe content exhibit lower weight loss, suggesting greater resistance to decomposition compared to those with higher Ni content, which is consistent with the XRD analysis results.

To further determine the composition of the materials, X-ray photoelectron spectroscopy (XPS) analysis was performed. As shown in Fig. 2d, Table 1, and Table 2, the XPS spectra in the range of 0–1000 eV for different materials revealed the presence of Fe, Ni, C, N, and O elements. Moreover, high-resolution XPS spectra more clearly identified the binding energy peaks of Fe 2p and Ni 2p in different materials. As illustrated in Fig. 3a, b, the binding energy peaks of Fe 2p1/2 [Fe(II)], Fe 2p3/2 [Fe(II)], and Fe 2p3/2 [Fe(III)] from Fe-MOFs, as well as Ni 2p1/2 [Ni(0)], Ni 2p3/2 [Ni(II)], and Ni 2p3/2 [Ni(0)] from Ni-MOFs, were present in Ni/Fe (3:1) MOFs, Ni/Fe (1:3) MOFs, and Ni/Fe (1:1) MOFs. These results confirm the successful synthesis of Fe-MOFs, Ni-MOFs, and Ni/Fe MOFs.

The porosity of the prepared materials was evaluated by N_2 adsorption–desorption isotherms at 77 K, as shown in Fig. 4a–e. It can be observed that Fe-MOFs follow a typical type IV isotherm with a significant hysteresis loop, indicating the presence of mesopores. Ni-MOFs exhibit a typical type II isotherm, indicative of multilayer adsorption on the surface of

non-porous solids. The adsorption–desorption isotherms of Ni/Fe MOFs show characteristics similar to both type II and type IV isotherms, suggesting that Ni/Fe MOFs combine the features of Fe-MOFs and Ni-MOFs,

Table 1 | The content of each element in different materials

Materials	Ni (%)	Fe (%)	C (%)	N (%)	O (%)
Fe-MOFs	-	61.85	20.04	2.79	15.31
Ni-MOFs	14.69	-	43.38	6.24	35.69
Ni/Fe (3:1) MOFs	20.83	8.42	23.68	3.31	43.76
Ni/Fe (1:1) MOFs	29.48	12.72	10.76	1.64	45.40
Ni/Fe (1:3) MOFs	14.49	28.89	11.23	1.28	44.12

Elemental compositions were determined by XPS full-spectrum quantitative analysis (after binding energy correction, peak areas were fitted using Avantage software), with an error margin of ±0.5%.

Table 2 | The bond energy of elements in XPS varies with different materials

Materials	Ni (eV)	Fe (eV)	C (eV)	N (eV)	O (eV)
Fe-MOFs	-	710.15	284.8	399.11	528.9
Ni-MOFs	855.26	-	284.8	399.25	531.78
Ni/Fe (3:1) MOFs	855.02	709.73	284.8	399.22	530.76
Ni/Fe (1:1) MOFs	855.39	712.49	284.8	399.14	530.82
Ni/Fe (1:3) MOFs	855.52	710.61	284.8	399.05	530.64

thereby confirming the successful synthesis of the material, consistent with previous characterization results. Additionally, the specific surface area and pore volume of each material were determined using the BET method, as shown in Table 3. The results indicate that the specific surface area and pore volume of Ni/Fe MOFs decrease due to the incorporation of Ni^{2+}, while the pore diameter increases. This may be attributed to the attached Ni^{2+} and Fe^{2+} molecules occupying some of the pore space, thereby reducing the pore volume and surface area[42,43].

Dye screening

Under identical conditions, the adsorption of eight different dyes by five Ni/Fe-MOFs with various molar ratios was evaluated, as depicted in Fig. 5a–e. Quantitative analysis of the adsorption data revealed significant trends. It was observed that Fe-MOFs exhibited exceptional adsorption capacities for EY and AF, while Ni-MOFs showed outstanding adsorption capabilities for NR and MG. Ni/Fe (3:1) MOFs demonstrated excellent adsorption performance for NR and AF, whereas Ni/Fe (1:1) MOFs and Ni/Fe (1:3) MOFs both exhibited superior adsorption capacities for AF and PB.

Moreover, comparative analysis indicated that among the five synthesized MOFs, higher Ni content resulted in better adsorption capacity for NR, whereas higher Fe content enhanced the adsorption capacity for AF. Further analysis reveals that the incorporation of Ni^{2+} into the MOF framework significantly alters the surface charge distribution and pore structure of the material. Specifically, Fe-MOFs exhibit a high specific surface area (281 m^2/g), which provides abundant active sites that facilitate the efficient adsorption of anionic dyes containing $-SO_3^-$ groups (e.g., EY) via electrostatic attraction. In contrast, despite their relatively low specific surface area (0.5 m^2/g), Ni-MOFs demonstrate superior selectivity for cationic dyes (e.g., NR) due to the strong Ni^{2+}–N coordination interactions. For Ni/Fe

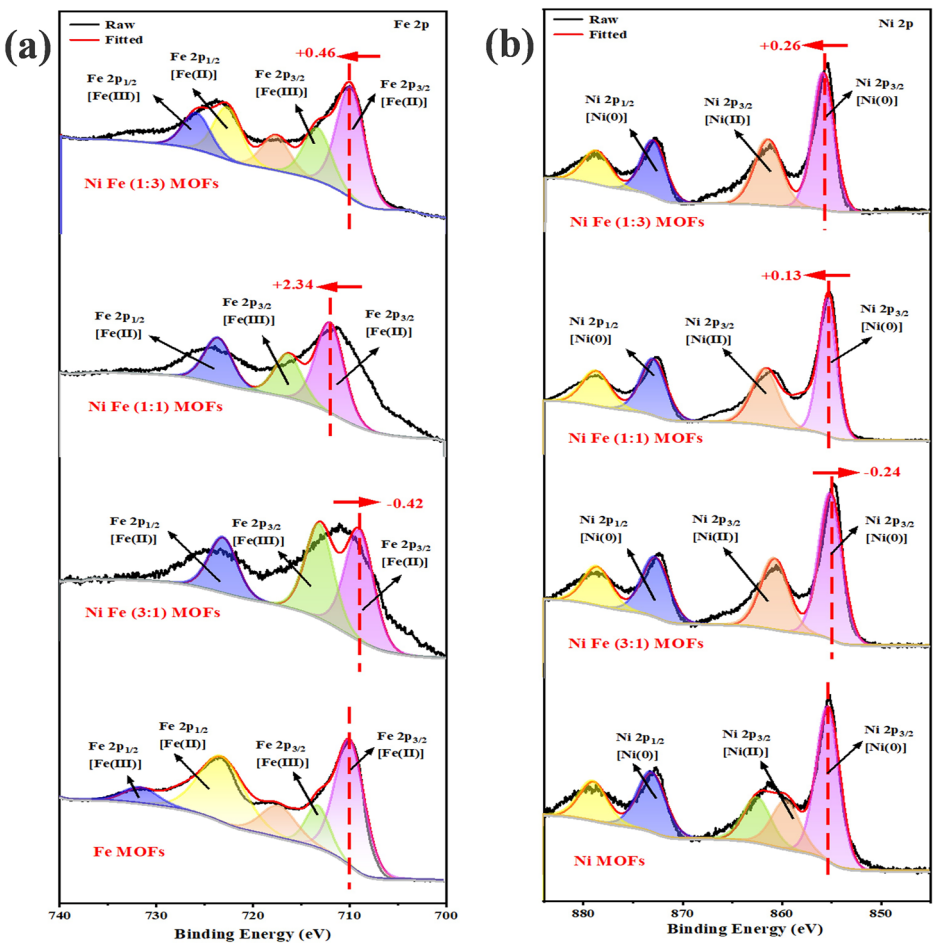

Fig. 3 | High-resolution XPS analysis of Fe and Ni oxidation states. a Fe 2p spectra for Fe-MOFs (Fe^{2+}/Fe^{3+} peaks at 710.15 and 712.49 eV) and Ni/Fe-MOFs. **b** Ni 2p spectra for Ni-MOFs (Ni^{2+} at 855.26 eV) and Ni/Fe-MOFs. Synergistic coordination between Ni and Fe is evident in bimetallic MOFs.

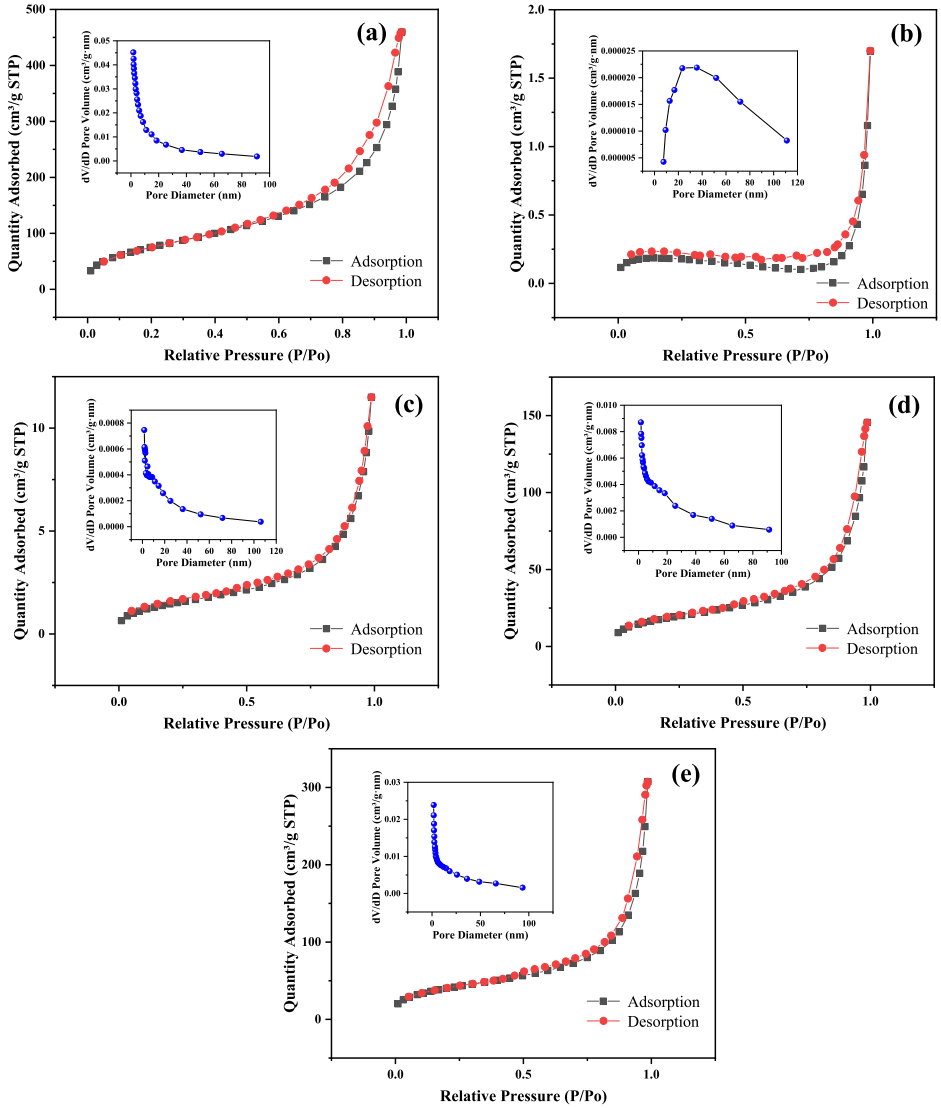

Fig. 4 | Porosity analysis of MOFs via nitrogen adsorption–desorption. BET isotherms for **a** Fe-MOFs (Type IV, mesoporous), **b** Ni-MOFs (Type II, non-porous), **c** Ni/Fe (3:1) MOFs (mixed Type II/IV), **d** Ni/Fe (1:1) MOFs, and **e** Ni/Fe (1:3) MOFs. Surface areas decrease with Ni incorporation, while pore sizes increase due to metal ion occupation.

Table 3 | Gas adsorption parameters of different materials

Materials	Surface area (m^2/g)	Pore volume (cm^3/g)	Aperture size (nm)
Fe-MOFs	281.2763	0.7006	10.0582
Ni-MOFs	0.5369	0.0022	44.7778
Ni/Fe (3:1) MOFs	5.3569	0.0170	13.2937
Ni/Fe (1:1) MOFs	67.1050	0.2160	13.8383
Ni/Fe (1:3) MOFs	144.0270	0.4655	13.8579

(1:1) MOFs, the synergistic effect of the bimetallic active sites (Fe–O–Ni clusters) and the presence of a well-developed mesoporous structure collectively enhance their adsorption performance for AF. These findings highlight that tuning the Ni/Fe ratio serves as a critical parameter for achieving selective dye adsorption in MOFs, as this strategy effectively modulates both surface charge distribution and pore structure, ultimately optimizing overall adsorption performance. By integrating structural characterization with adsorption data, it was concluded that each of the five materials exhibited exceptional adsorption for two specific dyes. Notably, Fe-MOFs, Ni-MOFs, and Ni/Fe (1:1) MOFs displayed significant structural differences, and the dyes they selectively adsorbed varied. This finding underscores the high selectivity of Ni/Fe bimetallic MOFs in dye adsorption and highlights the crucial role of structural modulation in influencing adsorption behavior.

Therefore, the design and synthesis of Ni/Fe-MOFs provide valuable insights for dye wastewater treatment. Preliminary selection includes Fe-MOFs for the adsorption of EY, Ni-MOFs for the adsorption of NR, and Ni/Fe (1:1) MOFs for the adsorption of AF as adsorption models for further in-depth adsorption performance studies.

Optimization of adsorption conditions

EY, NR, and AF reach adsorption equilibrium at different concentrations, thus, their optimal concentration ranges vary. The effect of the initial concentration of each dye on adsorption was investigated under the following conditions: adsorbent dosage of 10 mg, solution volume of 8 mL, shaking time of 30 min, and solution pH of 6.0. The impact of the initial concentration of EY on adsorption is shown in Fig. 6a. Initially, when the dye concentration ranges from 10 to 150 mg/L, the adsorption amount increases sharply; however, due to the limited number of unoccupied binding sites, a slower increase is observed when the initial dye concentration increases from 150 to 300 mg/L. Saturation is achieved when the initial dye concentration exceeds 300 mg/L. For NR, as shown in Fig. 6b, the adsorption amount increases sharply within the range of 10–1200 mg/L; again, due to the limited number of unoccupied binding sites, a slower increase is

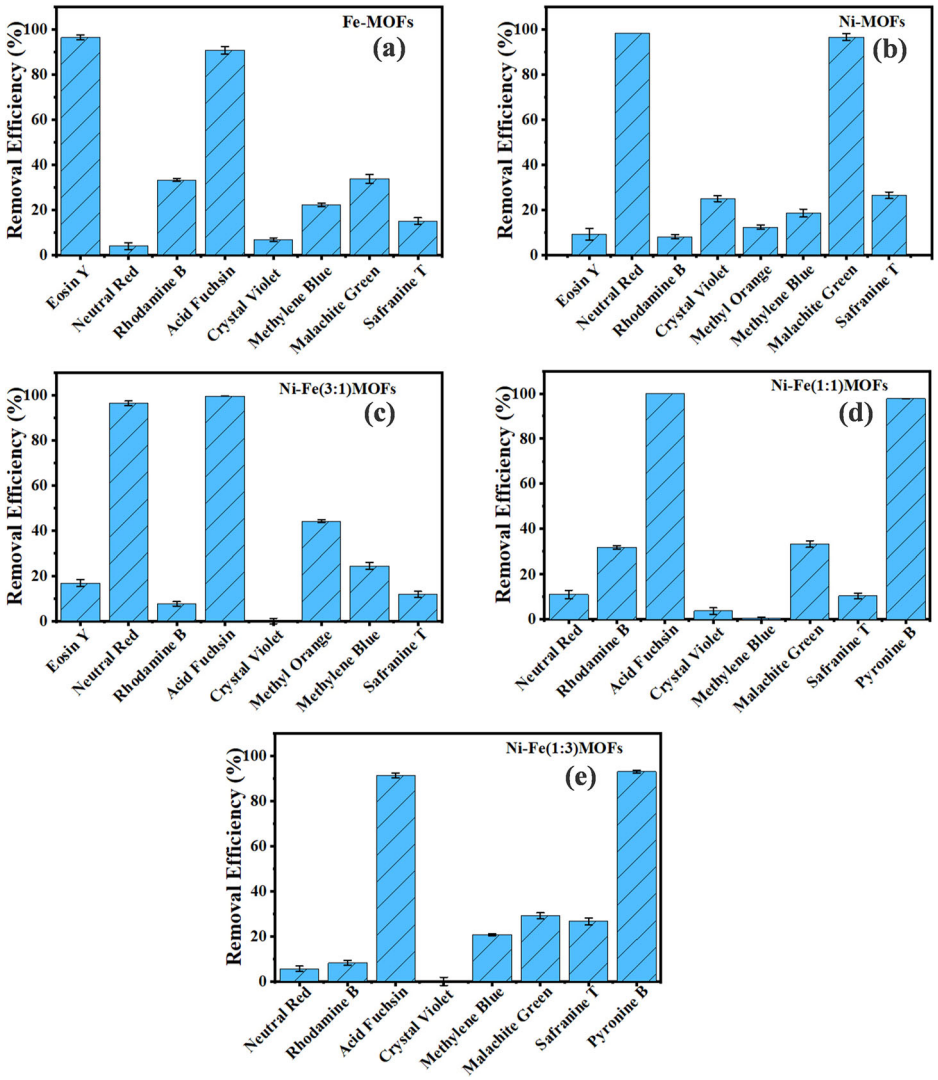

Fig. 5 | Selective adsorption of dyes by Ni/Fe-MOFs. Adsorption capacities of **a** Fe-MOFs, **b** Ni-MOFs, **c** Ni/Fe (3:1) MOFs, **d** Ni/Fe (1:1) MOFs, and **e** Ni/Fe (1:3) MOFs for eight dyes. Fe-MOFs favor anionic dyes (e.g., EY), Ni-MOFs adsorb cationic dyes (e.g., NR), and Ni/Fe (1:1) MOFs show enhanced AF uptake due to synergistic effects.

observed when the initial dye concentration increases from 1200 to 3000 mg/L. Saturation is achieved when the initial dye concentration exceeds 3000 mg/L. For AF, as shown in Fig. 6c, the adsorption amount increases sharply within the range of 10–200 mg/L; a slower increase is observed when the initial dye concentration increases from 200 to 300 mg/L due to the limited number of unoccupied binding sites, reaching adsorption equilibrium between 300 and 500 mg/L. To better study the material characteristics and adsorption performance, Fe-MOFs were selected for subsequent experiments at an initial EY concentration of 150 mg/L, Ni-MOFs at an initial NR concentration of 1200 mg/L, and Ni/Fe (1:1) MOFs at an initial AF concentration of 200 mg/L.

To investigate the effect of adsorbent dosage on the adsorption of EY on Fe-MOFs, NR on Ni-MOFs, and AF on Ni/Fe (1:1) MOFs, initial concentrations of 150, 1200, and 200 mg/L were used for EY, NR, and AF, respectively. The adsorbent dosage was varied using the same gradient (2, 5, 8, 10, 15, 20, and 25 mg), with a solution volume of 8 mL, shaking time of 30 min, and solution pH of 6.0. As shown in Fig. 8d–f, the removal efficiency of all three dyes increased rapidly as the adsorbent dosage increased from 2 to 10 mg. This increase is likely due to the composite materials having a larger specific surface area and more available adsorption sites, providing more sites for dye adsorption and thus increasing the dye removal rate. However, as the adsorbent dosage continued to increase, the rate of dye removal began to slow and eventually stabilized. It was observed that the removal rate for EY stabilized at 20 mg, for NR at 15 mg, and for AF at 20 mg. Therefore, 20 mg of Fe-MOFs, 15 mg of Ni-MOFs, and 20 mg of Ni/Fe (1:1) MOFs were selected for subsequent adsorption experiments.

To determine the optimal adsorption time for the composite materials on dye adsorption, identifying the optimal adsorption time is a crucial parameter for the adsorbent. The effect of adsorption time on the adsorption of EY on Fe-MOFs, NR on Ni-MOFs, and AF on Ni/Fe (1:1) MOFs was investigated under the conditions of initial dye concentrations of 150, 1200, and 200 mg/L, respectively, adsorbent dosages of 20, 15, and 20 mg, solution volume of 8 mL, and solution pH of 6.0. The shaking adsorption times studied were 5, 10, 20, 30, 45, 60, 75, and 90 min. The results, as shown in Fig. 6g–i, indicate that the adsorption rates and adsorption amounts of Fe-MOFs, Ni-MOFs, and Ni/Fe (1:1) MOFs on the dyes did not exhibit significant changes with varying adsorption times and reached equilibrium within 5 min. Therefore, 5 min was selected as the optimal adsorption time for further studies.

In adsorption systems, pH is also a crucial factor influencing adsorption performance. The effect of solution pH on the adsorption of dyes by Fe-MOFs, Ni-MOFs, and Ni/Fe (1:1) MOFs was studied under the conditions of initial dye concentrations of 150, 1200, and 200 mg/L, respectively, adsorbent dosages of 20, 15 and 20 mg, solution volume of 8 mL, and shaking adsorption time of 5 min. As shown in Fig. 7a–c, the adsorption efficiencies of Fe-MOFs and Ni-MOFs for EY and NR remained largely unchanged with variations in solution pH, indicating that their surface charge states were relatively stable across the investigated pH range.

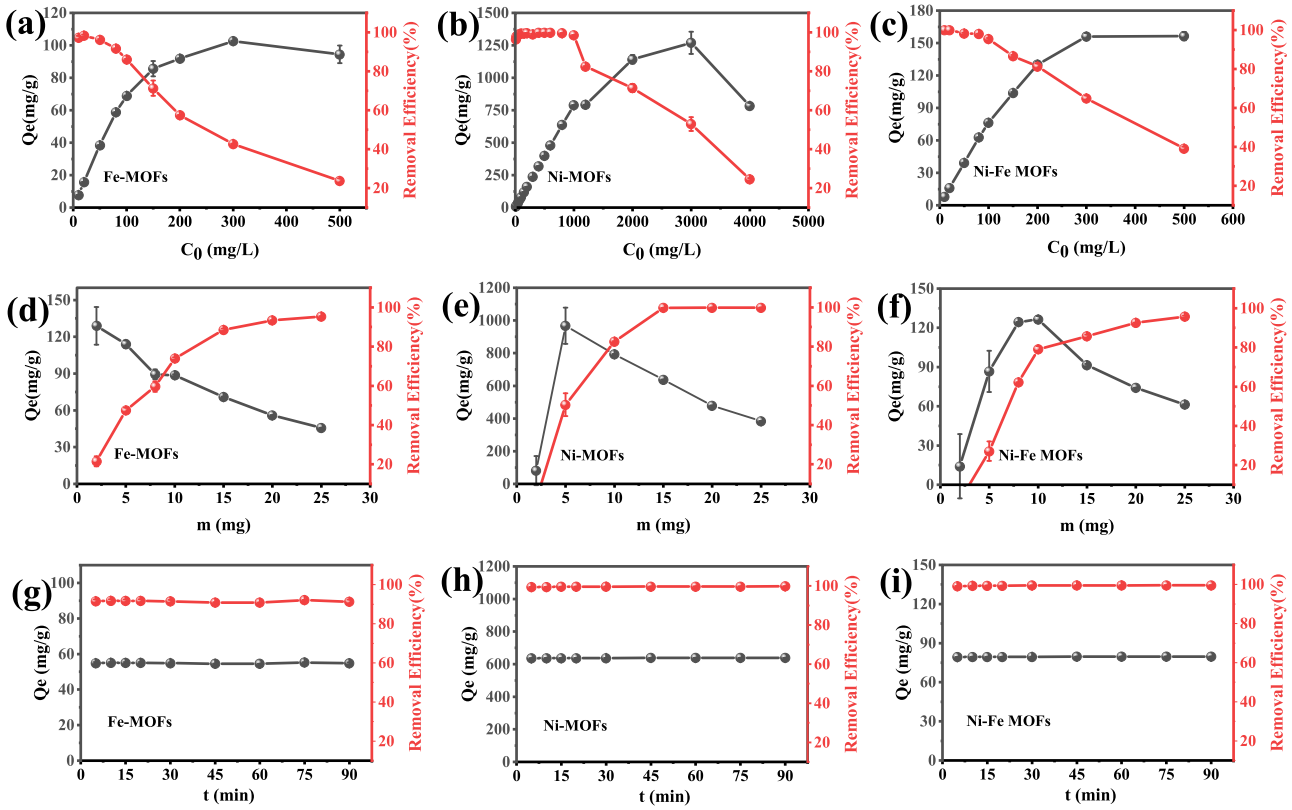

Fig. 6 | Optimization of dye adsorption parameters: initial concentration, adsorbent dosage, and time. a–c Initial Dye Concentration Optimization: **a** Fe-MOFs for EY adsorption: Adsorption capacity increases with EY concentration (10–300 mg/L), reaching equilibrium at 150 mg/L. **b** Ni-MOFs for NR adsorption: Adsorption capacity rises sharply with NR concentration (10–3000 mg/L), saturating at 1200 mg/L. **c** Ni/Fe (1:1) MOFs for AF adsorption: Adsorption capacity increases with AF concentration (10–500 mg/L), achieving equilibrium at 200 mg/L. **d–f** Adsorbent Dosage Optimization: **d** Fe-MOFs: Removal efficiency increases with dosage (2–25 mg), stabilizing at 20 mg (90% removal). **e** Ni-MOFs: Optimal dosage for NR removal is 15 mg (>99% efficiency). **f** Ni/Fe (1:1) MOFs: Maximum AF removal (97%) observed at 20 mg dosage. **g–i** Adsorption Time Optimization: **g** Fe-MOFs: EY adsorption equilibrium achieved within 5 min (Qe = 54.92 mg/g). **h** Ni-MOFs: NR adsorption completes in 5 min (Qe = 636.31 mg/g). **i** Ni/Fe (1:1) MOFs: AF adsorption reaches equilibrium in 5 min (Qe = 79.30 mg/g).

However, the adsorption efficiency of Ni/Fe (1:1) MOFs for AF exhibited slight fluctuations with increasing pH, reaching its maximum under near-neutral conditions. This behavior can be attributed to the competitive adsorption between H^+ ions and AF molecules at lower pH values, where H^+ ions partially occupy the active adsorption sites on the adsorbent, thereby limiting its adsorption potential for AF. Under near-neutral conditions, the enhanced ionization state of the dye molecules and the optimized surface charge of the adsorbent contribute to the highest adsorption efficiency.

To further elucidate the underlying mechanism, zeta potential measurements were conducted for all materials at pH 3, 4, 6, and 7, as shown in Supplementary Fig. 1. The results indicate that the points of zero charge (pHPZC) of Fe-MOFs, Ni-MOFs, and Ni-Fe (3:1) MOFs are 3.95, 4.84, and 4.86, respectively. These findings suggest that the surface charge states of MOFs undergo significant adjustments in response to pH variations, thereby influencing their electrostatic interactions with dye molecules. Moreover, previous studies have reported that the pKa values of EY, NR, and AF are 2.1, 6.8, and 3.5, respectively[44–46]. Since the pKa value dictates the ionization state (ionic or neutral) of a dye under different pH conditions, it plays a crucial role in determining its binding affinity toward the adsorbent. Consequently, it can be inferred that Fe-MOFs, Ni-MOFs, and Ni/Fe (1:1) MOFs possess stable structures and strong resistance to interference, making them suitable for use across a wide pH range.

In dye wastewater, not only are organic dyes present, but also various coexisting ions such as Na, K, and Cl. The effect of salt ions on the adsorption capacity of Fe-MOFs, Ni-MOFs and Ni/Fe (1:1) MOFs was investigated under the conditions of initial dye concentrations of 150, 1200, and 200 mg/L, respectively, adsorbent dosages of 20, 15, and 20 mg, solution volume of 8 mL, shaking adsorption time of 5 min, and solution pH of 6.0. Figure 7d–f illustrates the adsorption capacity of Fe-MOFs, Ni-MOFs, and Ni/Fe (1:1) MOFs for dyes in the presence of three different concentrations (5, 20, 50 mg/L) of salt ions (Na^+, K^+, Cl^-). The coexisting salt ions exhibited a very slight inhibitory effect on the adsorption of EY and AF dye molecules, with removal efficiencies decreasing from 90% to 88% and from 97% to 94%, respectively, while having almost no impact on the adsorption of NR dye molecules. This is attributed to the competition between the coexisting ions and the dyes for adsorption sites on the surface of the composite materials. As the concentration of coexisting ions increases, the number of available adsorption sites decreases, resulting in a slight reduction in the electrostatic interactions between the dyes and the composite materials. Therefore, it can be concluded that Fe-MOFs, Ni-MOFs, and Ni/Fe (1:1) MOFs possess good resistance to ion interference and have potential applications in the practical treatment of dye wastewater.

Reusability

From the perspective of practical applications, stability and recyclability are crucial criteria for evaluating the performance of adsorbents. In this study, Fe-MOFs, Ni-MOFs, and Ni/Fe (1:1) MOFs were employed in five consecutive adsorption cycles. As illustrated in Fig. 9d, Fe-MOFs exhibited a significant reduction in EY removal efficiency from 93% to 50% during the second cycle, and maintained a steady removal rate of around 50% from the second to the fifth cycle. One possible reason for this phenomenon is the incomplete removal of adsorbed dye by 100 mM $NaBH_4$. However, Ni-MOFs and Ni/Fe (1:1) MOFs demonstrated a regeneration efficiency of over 90% for NR and AF across five cycles, indicating satisfactory recyclability.

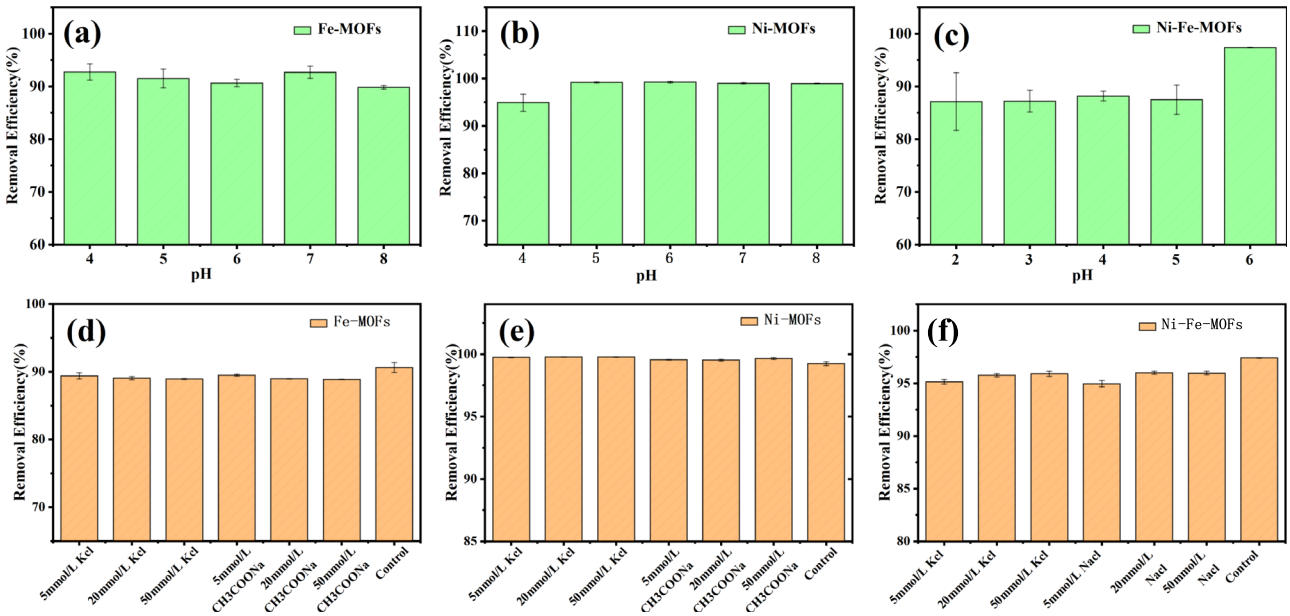

Fig. 7 | pH and ionic strength effects on dye adsorption. a–c pH-independent EY/NR adsorption, while AF removal peaks at pH 6 due to reduced H^+ competition. **d–f** Coexisting ions (Na^+, K^+, Cl^-) minimally affect adsorption, confirming strong anti-interference capability.

This might be attributed to the potentially superior regeneration stability of monometallic Ni-MOFs compared to monometallic Fe-MOFs, and the enhanced regeneration stability of bimetallic Ni/Fe (1:1) MOFs due to the incorporation of Ni. Therefore, Fe-MOFs, Ni-MOFs, and Ni/Fe (1:1) MOFs can be considered effective and recyclable adsorbents for dye treatment processes.

Selective adsorption of dyes in a binary system

Considering the coexistence of various dye molecules in actual wastewater, two dyes with excellent adsorption rates were selected based on the screening results. The conditions were set as follows: dosages of 20, 15, and 20 mg for Fe-MOFs, Ni-MOFs, and Ni/Fe (1:1) MOFs, respectively, with a solution volume of 8 mL, shaking adsorption time of 5 min, and solution pH of 6.0. The study investigated the simultaneous removal of EY (0–150 mg/L) and AF (0–150 mg/L) by Fe-MOFs, NR (0–1200 mg/L) and MG (0–1200 mg/L) by Ni-MOFs, and AF (0–200 mg/L) and PB (0–200 mg/L) by Ni/Fe (1:1) MOFs.

In a single system, Fe-MOFs exhibited adsorption rates of 91.5–98.9% for EY (37.5–150 mg/L) and 74.4–99.2% for AF (37.5–150 mg/L). In a binary system, as shown in Fig. 8a, b, the adsorption rates of Fe-MOFs for EY (37.5–150 mg/L) in the presence of AF (37.5–150 mg/L) were 59.4–97.4%, and for AF (37.5–150 mg/L) in the presence of EY (37.5–150 mg/L) were 51.3–98.4%. This indicates competitive adsorption in the binary system compared to the single system.

In a single system, Ni-MOFs exhibited adsorption rates of 99.2–99.7% for NR (300–1200 mg/L) and 97.8–98.8% for MG (300–1200 mg/L). In a binary system, as shown in Fig. 8c, d, the adsorption rates of Ni-MOFs for NR (300–1200 mg/L) in the presence of MG (300–1200 mg/L) were 98.4–99.4%, and for MG (300–1200 mg/L) in the presence of NR (300–1200 mg/L) were 89.6–97.9%. Thus, Ni-MOFs did not exhibit significant differences in adsorption rates for NR and MG between the single and binary systems.

In a single system, Ni/Fe (1:1) MOFs exhibited adsorption rates of 98.0–99.1% for AF (50–200 mg/L) and 85.5–98.6% for PB (50–200 mg/L). In a binary system, as shown in Fig. 8e, f, the adsorption rates of Ni/Fe (1:1) MOFs for AF (50–200 mg/L) in the presence of PB (37.5–150 mg/L) were 54.1–98.1%, and for PB (37.5–150 mg/L) in the presence of AF (50–200 mg/L) were 50.0–97.1%. This indicates competitive adsorption in the binary system compared to the single system.

Real sample analysis

To validate the efficacy of MOFs in removing dye molecules from water, adsorption tests were conducted using real water samples (tap water and irrigation water) and fruit and vegetable juices (cucumber juice, watermelon juice, pear juice, cantaloupe juice, orange juice, and white dragon fruit juice). As depicted in Fig. 9a–c, the results from these real samples indicate that Fe-MOFs, Ni-MOFs, and Ni/Fe (1:1) MOFs maintained a dye removal rate of over 91.53% across three different concentrations (low, medium and high) in both real water samples, showing minimal difference compared to their performance in deionized water.

Similarly, Fe-MOFs, Ni-MOFs, and Ni/Fe (1:1) MOFs achieved a dye removal rate of over 72.80% across three different concentrations in the six fruit and vegetable juice samples. These results suggest that, although certain external factors may slightly inhibit the adsorption efficiency of Fe-MOFs, Ni-MOFs, and Ni/Fe (1:1) MOFs, they still serve as effective adsorbents for the removal of EY, MG, and NR.

Adsorption isotherm and thermodynamic analysis

To investigate the adsorption equilibrium behavior of Fe-MOFs on EY, Ni-MOFs on NR, and Ni/Fe (1:1) MOFs on AF under stable temperatures, isothermal adsorption studies were conducted. Adsorption capacities of these three systems at different initial concentrations were analyzed using linear fitting of Langmuir, Freundlich, Temkin, Redlich-Peterson, and Dubinin-Rabushkevich models across four different temperatures (30, 40, 50, 60 °C). As shown in Fig. 10, the good fit of the Langmuir model confirms uniform surface and monolayer adsorption for Fe-MOFs, Ni-MOFs, and Ni/Fe (1:1) MOFs. The Freundlich model predicts multilayer adsorption occurring on heterogeneous surfaces with uneven energy levels. Additionally, the satisfactory fit of the mixed R-P model confirms applicability for both heterogeneous and homogeneous environments with Fe-MOFs and Ni/Fe (1:1) MOFs. The Temkin model, considering chemical adsorption between adsorbates and adsorbents, showed consistent fits across all temperatures, confirming uniform distribution of binding energies in dye adsorption characteristics. Therefore, isotherm data consistency with Langmuir, Temkin, and Redlich-Peterson models suggests monolayer-dominated adsorption processes for dyes.

To further characterize the adsorption process, thermodynamic parameters including Gibbs free energy change (ΔG), enthalpy change (ΔH), and entropy change (Δ*S*) were determined through processing and

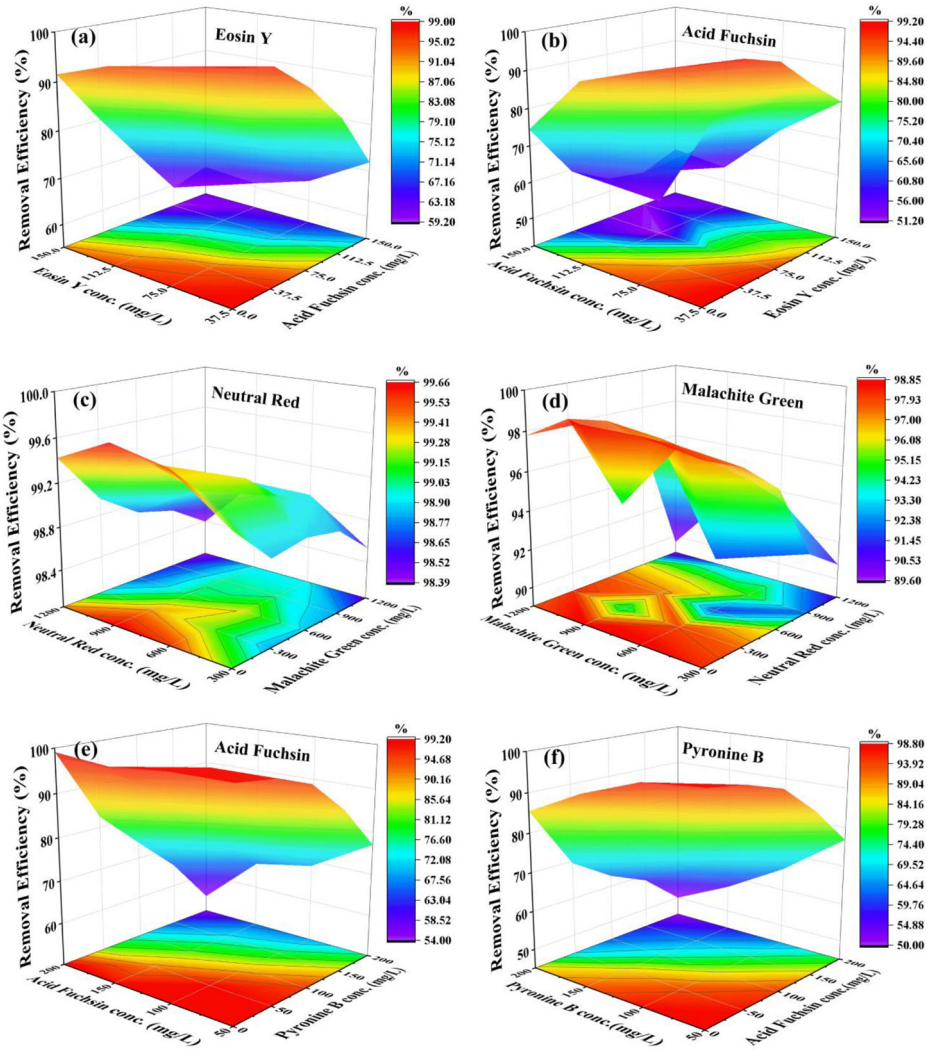

Fig. 8 | Competitive and synergistic adsorption in binary systems. Adsorption efficiency of Fe-MOFs for EY (**a**) and AF (**b**), Ni-MOFs for NR (**c**) and MG (**d**), Ni/Fe (1:1) MOFs for AF (**e**) and PB (**f**) in binary system dyes. **a**, **b** EY (37.5–150 mg/L) coexisting with AF (37.5–150 mg/L). Fe-MOFs exhibit competitive adsorption for EY and AF. **c**, **d** NR (300–1200 mg/L) coexisting with MG (300–1200 mg/L). Ni-MOFs synergistically adsorb NR and MG. **e**, **f** AF (50–200 mg/L) coexisting with PB (50–200 mg/L). Ni/Fe (1:1) MOFs show competition between AF and PB. Efficiency reductions in binary systems highlight selective interactions.

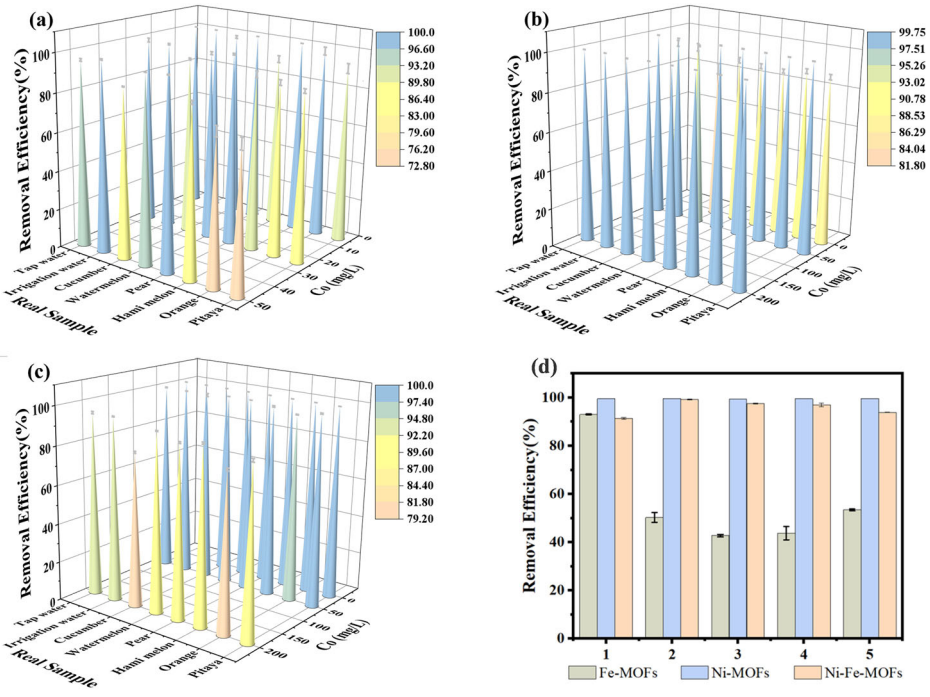

Fig. 9 | Real-sample performance and recyclability of MOFs. a Fe-MOFs adsorbed EY in actual samples; **b** Ni-MOFs adsorbed NR in real samples; **c** Ni/Fe (1:1) MOFs adsorbed AF in actual samples; **d** Recycling of materials. **a**–**c** Dye removal rates exceed 91.5% in real water samples (tap water and irrigation water) and 72.8% in fruit/vegetable juices (cucumber juice, watermelon juice, pear juice, cantaloupe juice, orange juice, and white dragon fruit juice). **d** Fe-MOFs lose 50% efficiency after regeneration, while Ni-MOFs and Ni/Fe (1:1) MOFs retain >90% efficiency over five cycles.

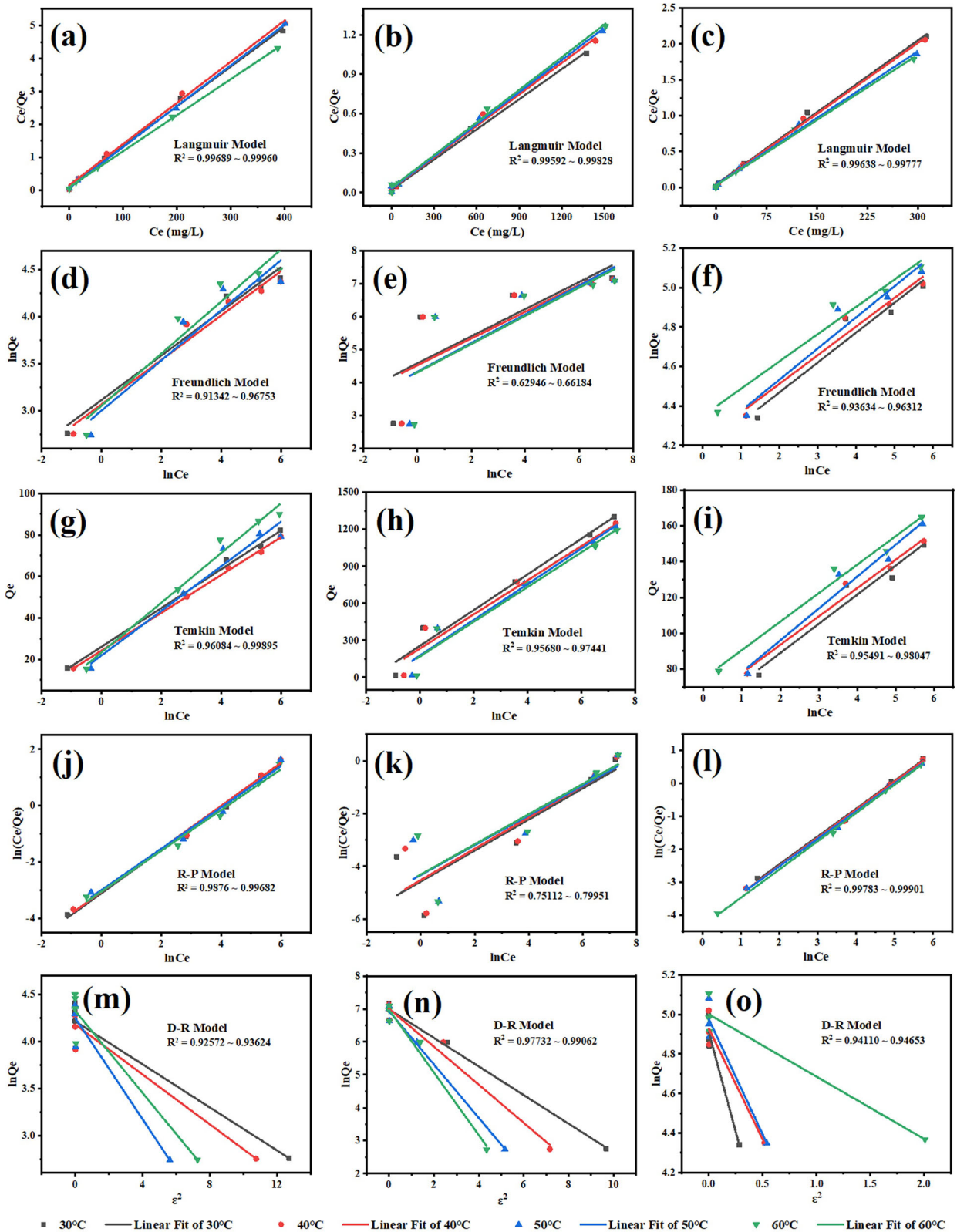

Fig. 10 | Adsorption isotherm models for dye uptake. Langmuir, Freundlich, Temkin, Redlich-Peterson, and Dubinin-Rabushkevich correspond to (**a**), (**d**), (**g**), (**j**), and (**m**) of Fe-MOFs respectively; (**b**), (**e**), (**h**), (**k**) and (**n**) corresponding to Ni-MOFs respectively; (**c**), (**f**), (**i**), (**l**) and (**o**) corresponding to Ni/Fe (1:1) MOFs respectively. Fe-MOFs fit Langmuir ($R^2 > 0.98$), Freundlich, and Temkin models. Ni-MOFs align with Langmuir (monolayer adsorption). Ni/Fe (1:1) MOFs follow mixed models, indicating heterogeneous surfaces.

analysis of adsorption experiments conducted at different temperatures. These parameters provide insights into the nature of the adsorption process. As shown in Table 4, ΔG decreases with increasing temperature, indicating favorable adsorption of EY on Fe-MOFs and AF on Ni/Fe (1:1) MOFs at higher temperatures. Conversely, Δ*G* increases with temperature, suggesting favorable adsorption of NR on Ni-MOFs at lower temperatures. ΔH > 0 indicates endothermic adsorption of EY on Fe-MOFs and AF on Ni/Fe (1:1) MOFs, with high values confirming strong interactions between dye and adsorbent. Conversely, ΔH < 0 indicates exothermic adsorption of NR on Ni-MOFs. Δ*S* > 0 suggests increased disorder during adsorption of EY on Fe-MOFs and AF on Ni/Fe (1:1) MOFs, while Δ*S* < 0 indicates decreased disorder during NR adsorption on Ni-MOFs. At temperatures ranging from 40 to 60 °C, Δ*G* < 0 indicates spontaneous adsorption of AF on Ni/Fe (1:1) MOFs.

Possible adsorption mechanism

To better understand the adsorption behavior of Fe-MOFs, Ni-MOFs, and Ni/Fe (1:1) MOFs towards dyes, exploring their underlying adsorption mechanisms is crucial. A comprehensive analysis of previous experimental data and characterization results allows for proposing rational mechanisms for dye removal. The possible adsorption mechanisms are illustrated in Fig. 11.

The adsorption mechanism of Fe-MOFs for EY primarily includes electrostatic interactions, hydrogen bonding, multilayer adsorption, and chemisorption. Given that EY is an anionic dye, the positive charges on the surface of Fe-MOFs (mainly from Fe^{2+} and Fe^{3+}) strongly attract the dye molecules through electrostatic interactions[44,47]. Additionally, hydroxyl groups on Fe-MOFs may form hydrogen bonds with carbonyl or hydroxyl groups in EY molecules, thereby enhancing the adsorption capacity[48]. The adsorption isotherms discussed earlier suggest that EY may undergo multilayer adsorption on the surface of Fe-MOFs, increasing the adsorption capacity. Moreover, the metal sites on the Fe-MOFs surface might react with active groups in EY molecules, forming chemical bonds, which further enhance the adsorption efficiency.

Table 4 | Thermodynamic parameters of the adsorption process of each material

Targets	*T* (°C)	*Kc*	Δ*G* (kJ/mol)	ΔH (J/mol)	Δ*S* (J/(mol·K))
EY	30	0.3599	2574.552	7007.988	14.166
	40	0.3412	2798.568		
	50	0.4038	2435.441		
	60	0.4511	2203.866		
NR	30	0.9457	140.539	−5098.009	−17.387
	40	0.8667	372.304		
	50	0.8120	559.401		
	60	0.7902	651.934		
AF	30	0.9604	101.810	7120.680	23.147
	40	1.0455	-115.861		
	50	1.1418	-356.073		
	60	1.2377	-590.408		

The adsorption mechanism of Ni-MOFs for NR primarily involves π–π interactions, electrostatic interactions, chemisorption, and van der Waals forces. The aromatic ring structure of NR molecules may strongly interact with the aromatic structures on the surface of Ni-MOFs through π–π interactions[49]. As a cationic dye, NR can undergo electrostatic adsorption with the negatively charged surface of Ni-MOFs. Metal sites on Ni-MOFs, such as Ni^{2+}, can form coordination bonds with nitrogen atoms or other active sites (e.g., amino groups) in NR molecules, thereby enhancing adsorption strength. Additionally, van der Waals forces between Ni-MOFs and NR molecules also play a supportive role during the adsorption process, contributing to the stability of the adsorption.

The adsorption mechanism of Ni/Fe (1:1) MOFs for AF includes synergistic effects, electrostatic interactions, hydrogen bonding, multilayer adsorption, and chemisorption. The synergistic effect of Ni and Fe metal elements results in the formation of additional active sites on the surface of Ni/Fe-MOFs, enhancing the adsorption of AF[50,51]. As an anionic dye, AF is attracted to the positive charges on the Ni/Fe-MOFs surface, primarily from Ni^{2+}, Fe^{2+}, and Fe^{3+}, facilitating the adsorption of anionic dye molecules. Hydrogen bonds may form between hydroxyl groups on the Ni/Fe-MOFs surface and hydroxyl or other oxygen-containing groups in AF molecules, increasing the adsorption strength. The isotherm models discussed earlier indicate that AF may undergo multilayer adsorption on the surface of Ni/Fe-MOFs, enhancing the adsorption capacity. Moreover, the metal sites on Ni/Fe-MOFs may form stable chemical bonds with active groups in AF molecules, further enhancing the adsorption efficiency.

To verify these adsorption mechanisms, BET and XRD analyses were conducted on Fe-MOFs, Ni-MOFs, and Ni/Fe (1:1) MOFs before and after adsorption. As depicted in Fig. 12a–f, combined with BET characterization pre- and post-adsorption, it was found that the N_2 adsorption–desorption isotherms of Fe-MOFs and Ni/Fe (1:1) MOFs did not change, and the pore size distribution curves in the inset also remained unchanged, confirming these materials possess a rich mesoporous structure[52,53]. Conversely, Ni-MOFs exhibited Type II adsorption isotherms, indicative of a microporous material, with alterations observed in both the isotherm type and pore size distribution curves post-adsorption, attributed to pore blockage from NR adsorption on the material surface, resulting in some nanoparticle aggregation, consistent with existing literature[54].

To further investigate the structural changes after adsorption, BET surface area and pore size were analyzed before and after dye adsorption

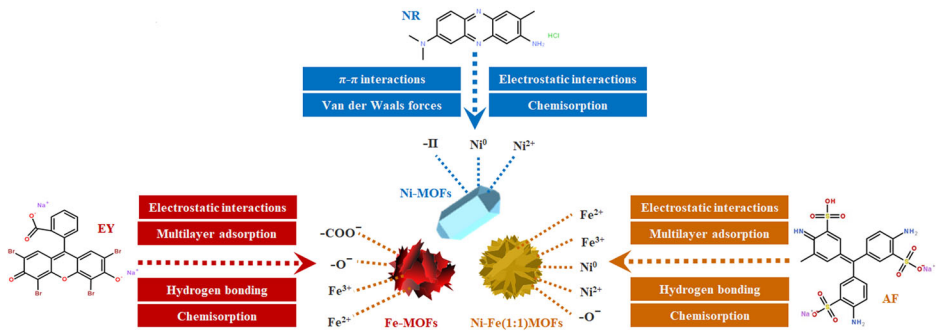

Fig. 11 | Proposed mechanisms for dye adsorption on MOFs. Fe-MOFs: Electrostatic attraction (Fe^{3+}/Fe^{2+}–EY^- –SO_3^-), hydrogen bonding (-OH in Fe-MOFs– –C=O/–OH in EY), multilayer adsorption (following the Freundlich isotherm), chemisorption (Fe sites–EY functional groups). Ni-MOFs: π–π stacking (NR aromatic rings–Ni-MOFs conjugated structures), electrostatic attraction (negative Ni-MOFs–cationic NR), Ni^{2+}–N/-NH_2 coordination, van der Waals stabilization. Ni/Fe (1:1) MOFs: Synergistic effects (Ni-Fe clusters), electrostatic attraction (Ni^{2+}/Fe^{3+}–AF^- –SO_3^-), hydrogen bonding (–OH on MOFs–AF relevant groups), multilayer adsorption (mixed isotherm), chemisorption (Ni/Fe sites–AF active groups). Fe-MOFs are red, Ni-MOFs are blue, and Ni/Fe (1:1) MOFs are orange.

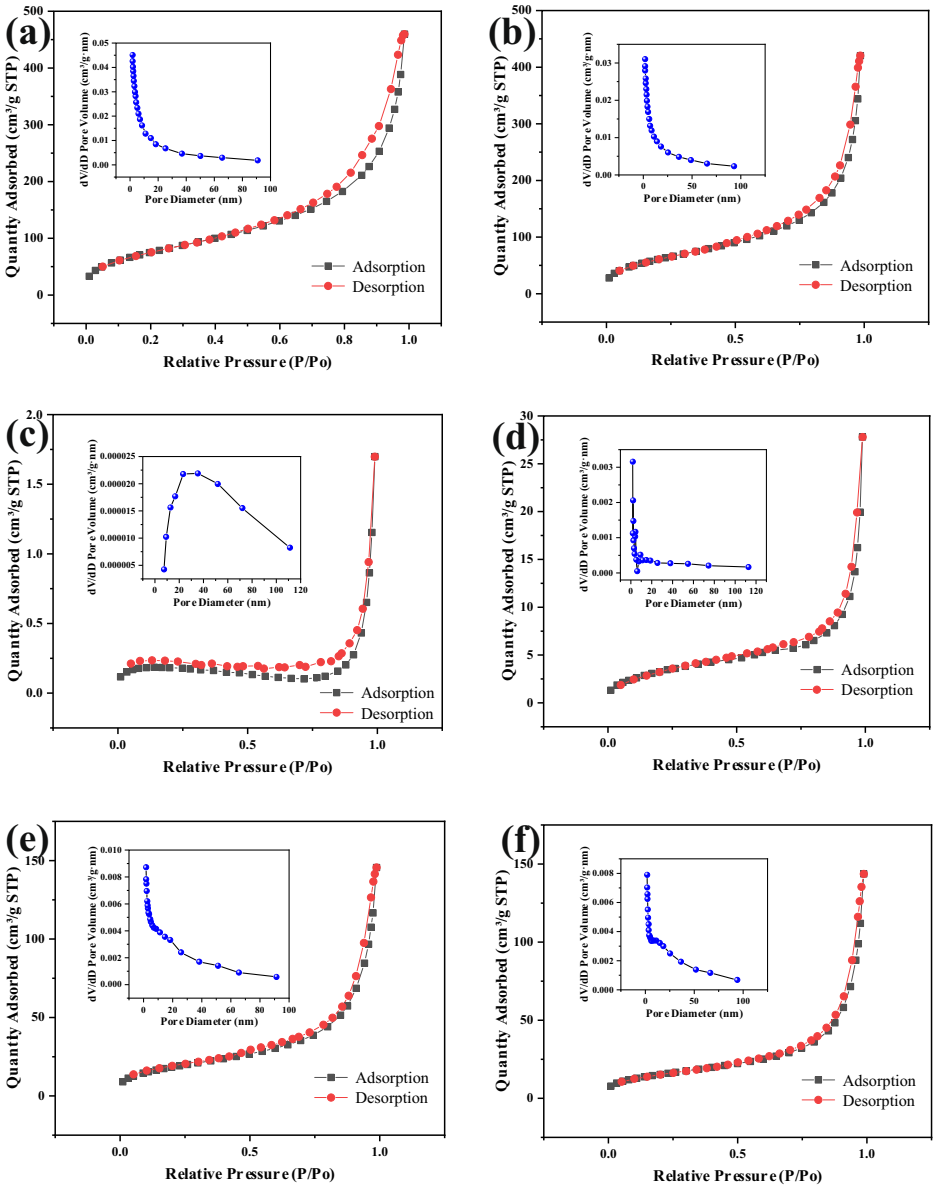

Fig. 12 | BET spectra before and after adsorption of dyes by different materials. a BET map of Fe-MOFs, **b** BET pattern of Fe-MOFs-EY; Fe-MOFs show reduced surface area (281 → 225 m^2/g) and pore size (10 → 0.6 nm) post-EY adsorption. **c** BET map of Ni-MOFs, **d** BET map of Ni-MOFs-NR; Ni-MOFs increase surface area (0.5 → 12.6 m^2/g) after NR adsorption. **e** BET map of Ni/Fe (1:1) MOFs, **f** BET map of Ni/Fe (1:1) MOFs–AF; Ni/Fe (1:1) MOFs retain mesopores (56 m^2/g, 16 nm) post-AF adsorption.

(Supplementary Table 2). For Fe-MOFs, which adsorbed EY (an anionic dye), the surface area decreased by 20.0% (from 281.28 to 225.07 m^2/g) and the pore size was dramatically reduced by 93.9% (from 10.06 to 0.61 nm), indicating significant pore blockage due to dye deposition. In contrast, Ni-MOFs, which adsorbed NR (a cationic dye), exhibited a remarkable increase in surface area of 2246.2% (from 0.54 to 12.60 m^2/g) alongside a 60.7% reduction in pore size (from 44.78 to 17.61 nm), suggesting that NR adsorption may have induced a reorganization of the framework, enhancing external surface accessibility while reducing larger mesopores. Meanwhile, Ni/Fe (1:1) MOFs, which adsorbed AF (a neutral dye), showed a modest 16.1% decrease in surface area (from 67.11 to 56.28 m^2/g) coupled with a 17.1% increase in pore size (from 13.84 to 16.21 nm), implying that AF adsorption likely resulted in structural expansion or rearrangement rather than simple pore filling. These observations underscore the diverse adsorption behaviors of the different MOFs, which are closely linked to their unique structural characteristics and their interactions with specific dyes.

XRD patterns of the materials before and after adsorption were obtained, as shown in Fig. 13. The results indicate that Fe-MOFs and Ni/Fe (1:1) MOFs retain their crystalline structure post-adsorption, whereas Ni-MOFs exhibit partial loss of crystalline structure after adsorption. This suggests that the overall structure of Fe-MOFs and Ni/Fe (1:1) MOFs remains largely unchanged during the adsorption process, while the structure of Ni-MOFs undergoes significant alteration, consistent with the BET characterization results.

Further analysis of the surface charge characteristics of the five MOFs under different pH conditions was conducted using a Zeta potential measurement system to elucidate their critical role in dye adsorption selectivity (Supplementary Table 3 and Supplementary Fig. 1). At pH 6, Fe-MOFs exhibited an overall negative surface charge (Zeta potential = −6.71 mV, pHPZC = 3.95); however, localized Fe^{3+}-O^- sites (XPS Fe $2p_3/_2$ = 712.49 eV) facilitated the electrostatic attraction of EY^{2-} (pKa = 2.1), while hydrogen bonding (FT-IR 3429 cm^{-1}) further enhanced adsorption stability[48]. In contrast, Ni-MOFs displayed a weaker surface charge (Zeta potential = −2.28 mV, pHPZC = 4.84), and their adsorption of NR^+ (pKa = 6.7) was primarily governed by coordination bonding between Ni^{2+} and the amine group (XPS Ni $2p_3/_2$ = 855.39 eV), along with π–π interactions[49]. For Ni/Fe (1:1) MOFs, despite their Zeta potential of −6.49 mV (pHPZC = 4.86) causing electrostatic repulsion with AF^- (pKa = 3.5), the redox pair of Ni^{2+}/Fe^{3+} provided a synergistic adsorption effect. Additionally, their mesoporous structure facilitated chemical bonding and multilayer adsorption, contributing to efficient dye removal[50]. Moreover, increasing the Ni content (e.g., Ni/Fe = 1:3 MOFs, pHPZC =

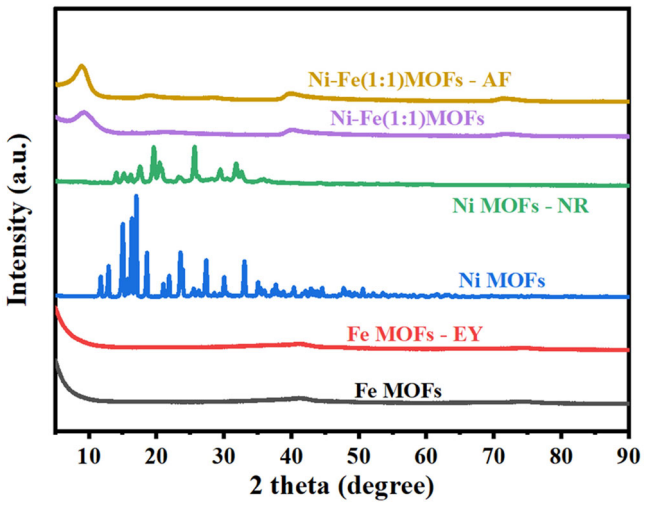

Fig. 13 | XRD spectra before and after adsorption of dyes by different materials. XRD patterns confirm the structural stability of Fe-MOFs and Ni/Fe (1:1) MOFs after adsorption. Ni-MOFs show partial amorphization due to NR-induced framework reorganization.

Table 5 | Comparison of the adsorption capacity of Fe-MOFs, Ni-MOFs, and Ni/Fe MOFs with other materials

Dye	Adsorbent	pH	Time (min)	Q_e (mg/g)	Reference
EY	MMT/PPy	7	20	112.9	56
	MCFs	2	10	3.96	57
	Fe-MOFs	6	5	54.92	This work
NR	MHPMs	7	10	61.5	58
	Activated Carbon fibers	9	120	20.7	59
	Ni-MOFs	6	5	636.31	This work
AF	CTS-MMT	5	90	3.208	45
	CMC/bentonite composite	2	60	253.2	60
	Ni/Fe MOFs	6	5	79.30	This work

5.07) effectively modulated the surface charge distribution, enabling better adaptation to different dye properties and ultimately optimizing overall adsorption performance.

Comparison with other adsorbents

Comparing with other adsorbent materials is crucial as it helps to evaluate the advantages and limitations of Fe-MOFs, Ni-MOFs, and Ni/Fe (1:1) MOFs in terms of dye adsorption performance. To comprehensively understand their adsorption capabilities, Table 5 summarizes the key parameters and performance metrics of these materials compared to other adsorbents, providing a clearer assessment of their potential and superiority in the field of dye adsorption.

Discussion

Based on different molar ratios of Ni/Fe bimetals, we synthesized five Ni/Fe-MOFs materials using a one-pot solvothermal method. These materials were characterized by SEM, XPS, BET, FT-IR, DSC, and XRD, and their adsorption performance for various dyes was preliminarily studied. The results indicate that as the molar ratio of Ni/Fe increases, the structures of the five materials transition from nanoflowers$_{(Fe\text{-}MOFs)}$ to nanospheres$_{(Ni/Fe(3:1)MOFs)}$ and then to rhombohedral blocks$_{(Ni\text{-}MOFs)}$. The specific surface area decreases from 281.3 $m^2/g_{(Fe\text{-}MOFs)}$ to 67.11 $m^2/g_{(Ni/Fe(1:1)\ MOFs)}$ and further to 0.5369 $m^2/g_{(Ni\text{-}MOFs)}$. We preliminarily selected Fe-MOFs for EY adsorption, Ni-MOFs for NR adsorption, and Ni/Fe (1:1) MOFs for AF adsorption for further optimization. Under optimal conditions, the maximum adsorption capacities for EY, NR, and AF were 54.92, 636.31, and 79.30 mg/g, respectively. Adsorption kinetics studies showed that the experimental data conformed to the pseudo-second-order kinetic model, and the equilibrium adsorption isotherms fitted the Langmuir model. Compared to single systems, in binary systems, Fe-MOFs exhibited competitive adsorption for EY and AF, Ni-MOFs showed synergistic adsorption for NR and MG, and Ni/Fe (1:1) MOFs demonstrated competitive adsorption for AF and PB. Thermodynamic results indicated that the adsorption processes for Fe-MOFs and Ni/Fe (1:1) MOFs were endothermic, while for Ni-MOFs, the process was exothermic. The adsorption mechanisms primarily involved multilayer adsorption and chemisorption, with hydrogen bonding, hydroxyl interactions, and electrostatic forces. Notably, these materials could be regenerated and reused over five cycles, maintaining high removal efficiency. Under optimal adsorption conditions, when applied to various real water samples and fruit and vegetable juices, the dye removal rates were maintained above 91.53% and 72.8%, respectively. The obtained materials were not only easy to regenerate and exhibited strong anti-interference capabilities but also showed excellent adsorption efficiency in environmental water samples and fruit and vegetable juices. Additionally, they demonstrated high selectivity in both single and binary dye adsorption systems. This study not only reveals the significant influence of the Ni/Fe ratio on the microstructure and adsorption performance of MOFs but also verifies the practical application potential of these MOFs in complex matrices through adsorption experiments of organic dyes in real water samples and fruit and vegetable juices. Our findings will provide theoretical support and technical guidance for the design of MOFs with high selectivity and adsorption performance, offering new insights for applications in environmental remediation and food safety.

Methods

Materials and chemicals

All reagents and chemicals were used as received without further purification. Nickel nitrate ($Ni(NO_3)_2{\bullet}6H_2O$), ferrous sulfate heptahydrate ($FeSO_4{\bullet}7H_2O$), potassium chloride (KCl), and sodium chloride (NaCl) were purchased from Xilong Scientific Co., Ltd. (Shanghai, China). Terephthalic acid ($C_8H_6O_4$), N,N-dimethylacetamide (C_4H_9NO), anhydrous ethanol (C_2H_6O), eosin Y (EY, $C_{20}H_6Br_4Na_2O_5$), neutral red (NR, $C_{15}H_{17}ClN_4$), acid fuchsin (AF, $C_{20}H_{17}N_3Na_2O_9S_3$), crystal violet (CV, $C_{25}H_{30}ClN_3$), methyl orange (MO, $C_{14}H_{14}N_3NaO_3$), methylene blue (MB, $C_{16}H_{18}N_3ClS$), malachite green (MG, $C_{23}H_{25}ClN_2$), safranine T (ST, $C_{20}H_{19}ClN_4$), pyronin B (PB, $C_{21}H_{27}ClN_2O$), anhydrous sodium acetate (CH_3COONa), and sodium hydroxide (NaOH) were obtained from Sinopharm Chemical Reagent Co., Ltd. (Shanghai, China). Triethanolamine ($C_6H_{15}NO_3$) was purchased from Aladdin Industrial Corporation (Shanghai, China).

Synthesis of Ni/Fe MOFs

Ni/Fe MOFs was prepared by a one-pot solvothermal method as shown in Fig. 14. Initially, $Ni(NO_3)_2{\bullet}6H_2O$ and $FeSO_4{\bullet}7H_2O$ were dissolved in 35 mL of water in an Erlenmeyer flask and magnetically stirred at room temperature for 0.5 h to obtain solution A. Subsequently, 0.3 mmol of terephthalic acid (H_2BDC) was dissolved in 35 mL of N,N-dimethylacetamide (DMAC) in another Erlenmeyer flask and magnetically stirred for 0.5 h to obtain solution B. DMAC was chosen as the solvent due to its high polarity and strong coordination ability, which facilitate the dissolution of Ni^{2+}, Fe^{2+} and H_2BDC, thereby promoting the coordination reaction and the formation of a stable MOF structure. Then, solution A was quickly added to solution B, followed by the addition of 1.6 mL of triethanolamine. This mixture was magnetically stirred at 80 °C for 8 h. After cooling the system to room temperature, magnetic separation was performed, and the resulting material was washed three times with ethanol, freeze-dried, and ground to

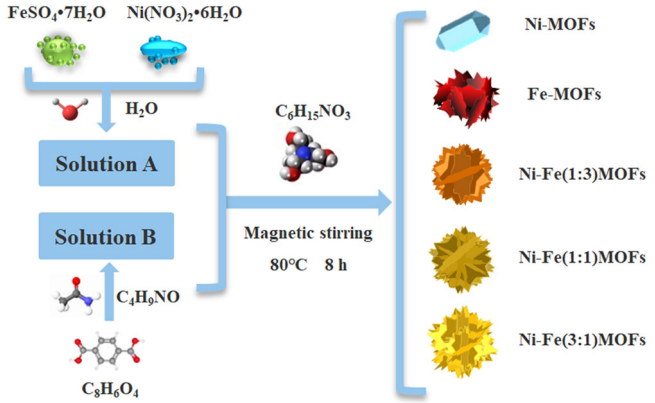

Fig. 14 | Preparation schematic diagram of different materials. Schematic of one-pot solvothermal synthesis. Ni^{2+}/Fe^{2+} and terephthalic acid coordinate in N,N-dimethylacetamide (DMAC) with triethanolamine, yielding tunable bimetallic MOFs.

Table 6 | The amount of metal used in the prepared material

Materials	$Ni(NO_3)_2•6H_2O$	$FeSO_4•7H_2O$
Fe-MOFs	-	0.8 mmol
Ni-MOFs	0.8 mmol	-
Ni/Fe (3:1) MOFs	0.6 mmol	0.2 mmol
Ni/Fe (1:1) MOFs	0.4 mmol	0.4 mmol
Ni/Fe (1:3) MOFs	0.2 mmol	0.6 mmol

obtain Ni/Fe MOFs powder. Freeze-drying was employed to remove residual solvent while preserving the porous structure of the MOFs, preventing collapse or aggregation that could occur with conventional drying methods. The quantities of $Ni(NO_3)_2•6H_2O$ and $FeSO_4•7H_2O$ used in the series of synthesized MOFs materials are listed in Table 6.

Characterization methods

The synthesized Ni/Fe MOFs materials were characterized using scanning electron microscopy (SEM), X-ray photoelectron spectroscopy (XPS), Brunauer–Emmett–Teller (BET) surface area analysis, Fourier-transform infrared spectroscopy (FT-IR), Thermogravimetric Analysis (TG-DSC), and X-ray diffraction (XRD) techniques to confirm successful synthesis and determine their related properties.

SEM (SM-6300, JEOL, Japan) was used to examine the morphological and microstructural features of the samples. XRD was conducted using a D8 Advance X-ray powder diffractometer (Co Kα radiation) to identify the crystalline structure and orientation, with a scanning range of 2θ = 5–90°, a scanning speed of 3°/min, and measurement duration exceeding 15 min. The analyzed materials were dried powders with particle sizes below 70 μm.

Surface elemental composition and chemical states were analyzed by XPS using a Thermo Fisher Scientific 250 Xi system, focusing on the C, N, O, Fe, and Ni elements. Nitrogen adsorption–desorption isotherms were obtained using an ASAP-2020 analyzer to assess surface area, pore volume, and pore size distribution (2–100 nm) based on BET analysis.

FT-IR spectra were acquired using a Thermo Nicolet iS10 spectrometer to identify functional groups and bonding information, with a spectral range of 400–4000 cm^{-1}, resolution of 4 cm^{-1}, signal-to-noise ratio of 50,000:1, and 64 scans per sample. The thermal behavior and stability were evaluated using a Netzsch STA 449 F5 TG-DSC analyzer from room temperature to 900 °C, at a heating rate of 10 °C/min.

Adsorption experiments

The adsorption performance of the five synthesized Ni/Fe-MOFs with different molar ratios was evaluated by adsorbing eight different dyes (eosin Y, neutral red, acid fuchsin, crystal violet, methyl orange, methylene blue, malachite green, safranine T, pyronin B) to identify their specific adsorption capabilities and establish adsorption models. Firstly, 10 mg of each material was weighed and placed in 10 mL centrifuge tubes, with eight sets prepared for each material. Subsequently, 8 mL of each 50 mg/L dye solution was added to each material. The centrifuge tubes containing the material-dye mixtures were then placed on a shaker and shaken at 300 rpm for 30 min. After shaking, the tubes were centrifuged at 9000 rpm for 10 min. The supernatant was then analyzed using a UV-Vis spectrophotometer to determine the removal efficiency and adsorption capacity. The calculations for removal efficiency and adsorption capacity are as follows[55]:

$$R(\%) = \frac{(C_0 - C_t)}{C_0} \times 100\% \quad (1)$$

$$Q_t\left(\frac{mg}{g}\right) = (C_0 - C_t) \times \frac{V}{m} \quad (2)$$

where C_0 (mg/L) is the initial concentration of the adsorbate, C_t (mg/L) is the concentration of the adsorbate at time t (min), V (L) is the volume of the solution in the adsorption system, m (mg) is the mass of the adsorbent, Q_t (mg/g) is the adsorption capacity at time t (min), and R (%) is the removal efficiency.

Single-factor adsorption experiments were conducted on the selected adsorption models to investigate their adsorption performance, as illustrated in Fig. 15. The influence of individual factors such as dye concentration, adsorbent mass, adsorption time, pH, salt concentration, and temperature on the adsorption performance was examined. The adsorbent was vigorously shaken with 8 mL of dye solution at the specified concentration in 10 mL centrifuge tubes, and the pH of the mixture was adjusted to the desired level using 1 mol/L NaOH and 1 mol/L HCl. The adsorption thermodynamics of EY, NR, and AF were studied at different temperatures. The residual concentrations of EY, NR, and AF were measured using UV-Vis spectrophotometry at their maximum absorption wavelengths of 517, 531, and 548 nm, respectively. The removal efficiency and adsorption capacity were then calculated accordingly.

To evaluate the regenerability of the adsorbents, desorption and recyclability studies were conducted using $NaBH_4$ as the eluent. Adsorbent desorption and recyclability analyses were performed by mixing 20 mg of Fe-MOFs with 150 mg/L EY, 15 mg of Ni-MOFs with 1200 mg/L NR, and 20 mg of Ni/Fe (1:1) MOFs with 200 mg/L AF. The mixtures were shaken at 300 r/min at room temperature for 5 min and then centrifuged at 9000 r/min for 10 min to collect the solids. The adsorbents loaded with EY, NR, and AF were regenerated by soaking in a 100 mM $NaBH_4$ eluent solution for 10 min, allowing for adsorbent regeneration and subsequent adsorption cycles.

Adsorption experiments were conducted following the same procedure as for single systems. Specifically, 20 mg of Fe-MOFs was added to mixtures containing 8 mL of combined EY and AF solutions. EY and AF were each tested at five concentrations (0, 37.5, 75, 112.5, and 150 mg/L), resulting in 25 different combined dye concentrations. Similarly, 15 mg of Ni-MOFs was added to mixtures containing 8 mL of combined NR and MG solutions. NR and MG were each tested at five concentrations (0, 300, 600, 900, and 1200 mg/L), resulting in 25 different combined dye concentrations. Additionally, 20 mg of Ni/Fe MOFs was added to mixtures containing 8 mL of combined AF and PB solutions. AF and PB were each tested at five concentrations (0, 50, 100, 150, and 200 mg/L), resulting in 25 different combined dye concentrations. Subsequently, adsorption was conducted for 5 min at the optimum solution pH and 25°C.

To rigorously evaluate the adsorption performance under conditions that closely mimic real-world scenarios, a diverse array of environmental matrices was employed. These matrices include tap water, irrigation water, and fruit and vegetable juices (namely cucumber, watermelon, pear, cantaloupe, orange, and dragon fruit juices). Prior to the experiments, the pH of all water samples was adjusted to 6 using hydrochloric acid, thereby

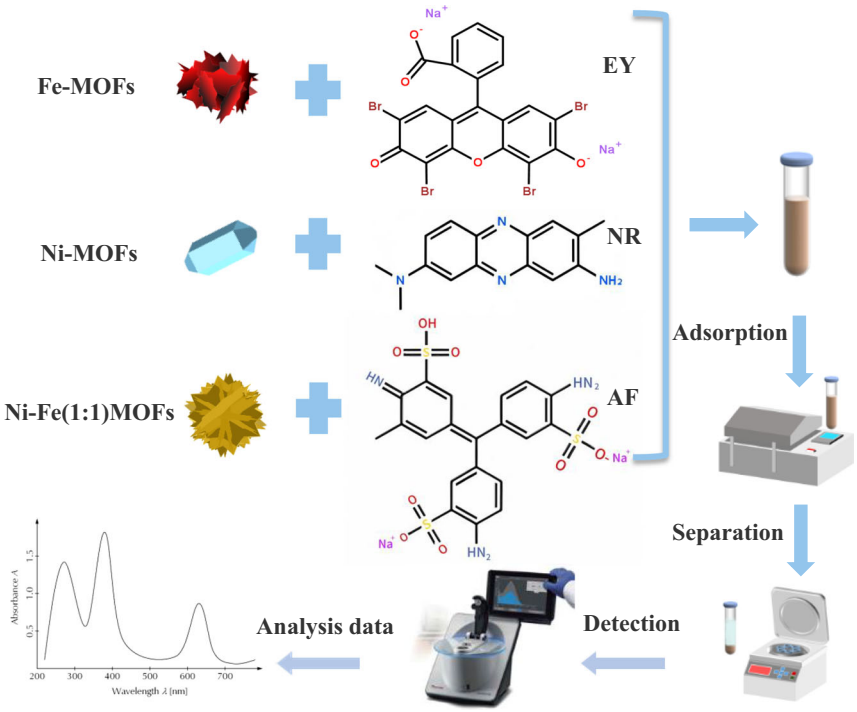

Fig. 15 | Schematic diagram of the adsorption process. The standard operating procedure for the adsorption experiment consists of the following steps: Mixing of materials and dyes: Accurately weighed adsorbents (Fe-MOFs, Ni-MOFs, or Ni/Fe (1:1) MOFs) are added together with a dye solution of a certain concentration (such as EY, NR, or AF) into a 10 mL centrifuge tube. Shaking adsorption: The mixture is placed in a constant temperature shaker (at 300 rpm), and shaken for a certain period of time at room temperature to achieve a rapid adsorption equilibrium. Centrifugal separation: Centrifuge at 9000 rpm for 10 min to separate the adsorbent from the supernatant, ensuring that the solid adsorbent is completely precipitated. Spectrophotometric analysis: Take the supernatant and use an ultraviolet-visible spectrophotometer (UV-Vis) to measure the residual dye concentration at specific wavelengths (EY: 517 nm, NR: 531 nm, AF: 548 nm), and calculate the removal efficiency (R%) and the adsorption capacity (Q).

mitigating pH-related variabilities in adsorption behavior. The experiments were conducted by spiking these matrices with three different concentration levels (low, medium, and high) of EY (5, 25, and 50 mg/L), NR (5, 50, and 200 mg/L), and AF (5, 50, and 200 mg/L). This experimental design was intended to simulate a range of aqueous and food-based environments, offering a comprehensive assessment of the adsorbent's efficacy across varied practical application conditions.

Data availability

Data will be made available on request.

Received: 2 March 2025; Accepted: 20 April 2025;
Published online: 29 April 2025

References

1. Oliveira, G. A. R. et al. A test battery for assessing the ecotoxic effects of textile dyes. *Chem. Biol. Interact.* **291**, 171–179 (2018).
2. Huang, C. T. & Chen, K. N. Self-curable aqueous polymeric dyes for printing and dyeing applications. *J. Appl. Polym. Sci.* **100**, 1919–1931 (2006).
3. Al-Etaibi, A. M., Alnassar, H. S. & El-Apasery, M. A. Dyeing of polyester with disperse dyes: part 2. synthesis and dyeing characteristics of some azo disperse dyes for polyester fabrics. *Molecules* **21**, 855–855 (2016).
4. Tkaczyk, A., Mitrowska, K. & Posyniak, A. Synthetic organic dyes as contaminants of the aquatic environment and their implications for ecosystems: a review. *Sci. Total Environ.* **717**, 137222 (2020).
5. Amchova, P., Kotolova, H. & Ruda-Kucerova, J. Health safety issues of synthetic food colorants. *Regul. Toxicol. Pharmacol.* **73**, 914–922 (2015).
6. Abe, F. R., Soares, A. M. V. M., Oliveira, D. P. D. & Gravato, C. Toxicity of dyes to zebrafish at the biochemical level: cellular energy allocation and neurotoxicity. *Environ. Pollut.* **235**, 255–262 (2018).
7. Berradi, M. et al. Textile finishing dyes and their impact on aquatic environs. *Heliyon* **5**, e02711 (2019).
8. Thomas, O. E., Adefolarin, A., Ana, G. & Odaibo, G. Determinants of knowledge associated with occupational hazards and perceived health problems among dye workers in Abeokuta, Nigeria. *J. Public Health Afr.* **14**, 1985 (2023).
9. Al-Tohamy, R. et al. A critical review on the treatment of dye-containing wastewater: ecotoxicological and health concerns of textile dyes and possible remediation approaches for environmental safety. *Ecotoxicol. Environ. Saf.* **231**, 113160 (2022).
10. Wang, X. et al. Carbon composite lignin-based adsorbents for the adsorption of dyes. *Chemosphere* **206**, 587–596 (2018).
11. Fengchun, J. et al. Efficient separation of dyes using two-dimensional heterogeneous composite membranes. *Water Res.* **247**, 120693–120693 (2023).
12. Lei, L. et al. Highly efficient magnetic separation of organic dyes from liquid water utilizing Fe3O4@graphene composites. *Mater. Res. Express* **6**, 106106–106106 (2019).
13. María, N. J. et al. Advances in the application of nanocatalysts in photocatalytic processes for the treatment of food dyes: a review. *Sustainability* **13**, 11676–11676 (2021).
14. Sher, F., Malik, A. & Liu, H. Industrial polymer effluent treatment by chemical coagulation and flocculation. *J. Environ. Chem. Eng.* **1**, 684–689 (2013).
15. Phetrak, A., Westerhoff, P. & Garcia-Segura, S. Low energy electrochemical oxidation efficiently oxidizes a common textile dye used in Thailand. *J. Electroanal. Chem.* **871**, 114301 (2020).
16. Srinivasan, S. & Sadasivam, S. K. Exploring docking and aerobic-microaerophilic biodegradation of textile azo dye by bacterial systems. *J. Water Process Eng.* **22**, 180–191 (2018).
17. Alam, A. M. S. et al. Comparative anaerobic decolorization of azo dyes by carbon-based membrane bioreactor. *Water* **13**, 1060–1060 (2021).
18. Kshaf, A. et al. A review on activated carbon modifications for the treatment of wastewater containing anionic dyes. *Chemosphere* **306**, 135566–135566 (2022).
19. Duc, P. T. et al. Adsorptive removal of anionic azo dye new coccine using silica and silica-gel with surface modification by polycation. *Polymers* **13**, 1536–1536 (2021).
20. Hassan, N., Shahat, A., El-Didamony, A., El-Desouky, M. G. & El-Bindary, A. A. Mesoporous iron oxide nano spheres for capturing organic dyes from water sources. *J. Mol. Struct.* **1217**, 128361 (2020).
21. Jiang, D. et al. The application of different typological and structural MOFs-based materials for the dyes adsorption. *Coord. Chem. Rev.* **380**, 471–483 (2019).

22. Dai, Y. et al. Recent progress in 1D MOFs and their applications in energy and environmental fields. *Adv. Colloid Interface Sci.* **321**, 103022 (2023).
23. Chen, L., Wang, H.-F., Li, C. & Xu, Q. Bimetallic metal–organic frameworks and their derivatives. *Chem. Sci.* **11**, 5369–5403 (2020).
24. Yu, J. et al. A novel mercapto-functionalized bimetallic Zn/Ni-MOF adsorbents for efficient removal of Hg(II) in wastewater. *J. Environ. Chem. Eng.* **12**, 113258 (2024).
25. Li, M. et al. One-step construction of Ti-In bimetallic MOFs to improve synergistic effect of adsorption and photocatalytic degradation of bisphenol A. *Sep. Purif. Technol.* **298**, 121658 (2022).
26. Zhao, Y. et al. Simple synthesis, characterization and mechanism of Fe/Zr bimetallic-organic framework for Cr (VI) removal from wastewater. *J. Environ. Chem. Eng.* **12**, 112040 (2024).
27. Mortazavi, B., Shahrokhi, M., Makaremi, M., Cuniberti, G. & Rabczuk, T. First-principles investigation of Ag-, Co-, Cr-, Cu-, Fe-, Mn-, Ni-, Pd- and Rh-hexaaminobenzene 2D metal-organic frameworks. *Mater. Today Energy* **10**, 336–342 (2018).
28. Zhang, L. et al. Two-dimensional magnetic metal-organic frameworks with the Shastry-Sutherland lattice. *Chem. Sci.* **10**, 10381–10387 (2019).
29. Yang, X., Tang, C., Hu, L., Zhou, Y. & Zhou, M. Catalytic oxidation of different lignin over Ni-MOFs based catalyst in oxygen: effect of catalysts and solvents. *Ind. Crops Products* **204**, 117305 (2023).
30. Zhu, G. et al. Application of Fe-MOFs in advanced oxidation processes. *Res. Chem. Intermed.* **45**, 3777–3793 (2019).
31. Jin, Y. et al. Surface functionalization of carbon cloth with conductive Ni/Fe-MOFs for highly efficient oxygen evolution. *Surf. Interfaces* **33**, 102294 (2022).
32. Mahya, S., Subhajit, N., Hwa, C. K. & Mahdi, N. M. Further insight into the conversion of a Ni-Fe metal-organic framework during water-oxidation reaction. *Inorg. Chem.* **61**, 5112–5123 (2022).
33. Huang, L., Shi, Y., Xiong, W., Ding, Y. & Zhang, Y. Q. Facile design of highly effective Fe-modified bimetallic Fe x –Ni 1−x -MOFs catalysts with rodlike structures for low-temperature NO reduction by CO. *J. Mater. Sci.* **56**, 1–15 (2021).
34. Changyan, G. et al. Precise regulation of defect concentration in MOF and its influence on photocatalytic overall water splitting. *Nanoscale* **14**, 15316–15326 (2022).
35. Trzmiel, J., Peksa, P., Ptak, M., Fedoruk, K. & Sieradzki, A. On the impact of metal ions proportion on physical properties of heterometallic metal-organic frameworks. *CrystEngComm* **22**, 4716–4722 (2020).
36. Pinghua, C. et al. Construction of ZIF-67/MIL-88(Fe, Ni) catalysts as a novel platform for efficient overall water splitting. *Int. J. Hydrog. Energy* **48**, 7170–7180 (2023).
37. Li, Y. et al. Trimetallic metal-organic framework derived carbon-based nanoflower electrocatalysts for efficient overall water splitting. *Adv. Mater. Interfaces* **6**, 1900290 (2019).
38. Chen, C. Hierarchical trimetallic Co-Ni-Fe oxides derived from core-shell structured metal-organic frameworks for highly efficient oxygen evolution reaction. *Appl. Catal. B. Environ.* **287**, 119953 (2021).
39. Jing, Y. et al. MOF-derived Co, Fe, and Ni co-doped N-enriched hollow carbon as efficient electrocatalyst for oxygen reduction reaction. *Chem. Eng. J.* **397**, 125539 (2020).
40. Zhang, Y. et al. Highly sensitive and selective toluene sensor of bimetallic Ni/Fe-MOFs derived porous NiFe2O4 nanorods. *Ind. Eng. Chem. Res.* **58**, 9450–9457 (2019).
41. Ahmad, K. et al. Engineering of Zirconium based metal-organic frameworks (Zr-MOFs) as efficient adsorbents. *Mater. Sci. Eng. B* **262**, 114766 (2020).
42. Zhi, S. X. et al. Hollow NiFe2O4 microspindles derived from Ni/Fe bimetallic MOFs for highly sensitive acetone sensing at low operating temperatures. *Inorg. Chem. Front.* **5**, 1107–1114 (2018).
43. Ahmad, K. et al. Effect of metal atom in zeolitic imidazolate frameworks (ZIF-8 & 67) for removal of Pb2+ & Hg2+ from water. *Food Chem. Toxicol.* **149**, 112008 (2021).
44. Sakr, M., Adly, M. S., Alalm, M. G. & Mahanna, H. Effective removal of acetamiprid and eosin Y by adsorption on pristine and modified MIL-101(Fe). *Environ. Sci. Pollut. Res. Int.* **31**, 41221–41245 (2024).
45. Cao, C.-Y., Zhang, T. & Cong, Q. Adsorption of acid fuchsin onto the chitosan–montmorillonite composite. *Mar. Georesources Geotechnol.* **35**, 799–805 (2017).
46. Singh, M. K., Pal, H., Koti, A. S. R. & Sapre, A. V. Photophysical properties and rotational relaxation dynamics of neutral red bound to β-xyclodextrin. *J. Phys. Chem. A.***108**, 1465–1474 (2004).
47. Maqsood, K. Synthesis and photocatalytic degradation efficiency of MgFe2O4@CuO nanocomposite for Bromophenol blue dye removal. *J. Chin. Chem. Soc.* **72**, 390 (2025).
48. Zhao, S. et al. An azine-based polymer derived hierarchically porous N–doped carbon for hydrophilic dyes removal. *J. Hazard. Mater.* **413**, 125299 (2021).
49. Singh, P., Ahmad, M. & Siddiqui, K. A. Ni-coordination polymer as potential remedial compound for efficient detection and seclusion of toxic aromatic dyes from contaminated water. *J. Mol. Struct.* **1274**, 134422 (2023).
50. Gu, N., Xu, Y., Yin, Y., Gao, X. & Zeng, Y. Synergistic desulfurization over Ni(II) and Fe sites in adsorbent Ni@MIL-100(Fe). *Microporous Mesoporous Mater.* **362**, 112804 (2023).
51. Abbas, S. et al. Cutting-edge metal-organic frameworks: revolutionizing the adsorptive removal of pharmaceutical contaminants from water. *Rev. Inorg. Chem.* https://doi.org/10.1515/revic-2024-0119 (2025).
52. Zhou, J. Facile preparation of magnetic COF-on-COF for rapid adsorption and determination of sulforaphane from cruciferous vegetables. *Foods* **13**, 409 (2020).
53. Ahmad, K. et al. MOFs@COFs composites: Advances, challenges, and multifunctional applications in emerging technologies. *Hybrid Adv.* **9**, 100419–100419 (2025).
54. Tao, Z., Pan, W., Gary, O. & Zuliang, C. Adsorption and fenton-like oxidation of ofloxacin in wastewater using hybrid MOF bimetallic Fe/Ni nanoparticles. *Chemosphere* **307**, 135936–135936 (2022).
55. Xu, D. et al. Synergistic adsorption and Fenton-like oxidation of neutral red by the combination of COFs and Co(OH)2 in chitosan hydrogel microspheres. *Sustain. Mater. Technol.* **43**, e01279 (2025).
56. Zhang, M., Chang, L., Zhao, Y. & Yu, Z. Fabrication, characterization and adsorption behavior of montmorillonite/polypyrrole nanocomposites for Eosin Y removal. *Polym. Bull.* **75**, 4881–4899 (2018).
57. Li, X. & Zhai, Q. Evaluation of eosin Y removal from aqueous solution using nano-mesoporous material MCFs: adsorption equilibrium, kinetics, and adsorption isotherms. *Int. J. Ind. Chem.* **11**, 55–67 (2020).
58. Chen, X. et al. Effect of embedded sodium polyacrylate chains on the adsorption mechanism of neutral red by magnetic particles. *Chem. Eng. Res. Des.* **127**, 223–235 (2017).
59. Ling, Z. et al. Coconut-based activated carbon fibers for efficient adsorption of various organic dyes. *RSC Adv.* **8**, 42280–42291 (2018).
60. Gong, N., Liu, Y. & Huang, R. Simultaneous adsorption of Cu 2+ and Acid fuchsin (AF) from aqueous solutions by CMC/bentonite composite. *Int. J. Biol. Macromol.* **115**, 580–589 (2018).

Acknowledgements

The research was supported by Beijing Natural Science Foundation (6242028), National Key Research and Development Program of China (2022YFF0606800), the Special Fund for the Industrial System Construction of Modern Agriculture of China (CARS-23-E03), National Center of Technology Innovation for Comprehensive Utilization of Saline-Alkali (GYJ2023004) and Central Public-interest Scientific Institution Basal Research Fund (No. IVF-BRF2024013).

Author contributions

D.X. and G.L. conceived the study, designed the methodology, conducted experiments, and wrote the original draft. X.C. conceptualized the framework, developed software tools, provided resources, supervised the

research, and conducted investigations. J.Z., Z.L., J.H., G.C., X.X., and Y.Z. performed formal analysis, validated data, and contributed to experimental investigations. J.W. and D.H.X. developed software, managed resources, coordinated the project, and secured funding. G.L. additionally supervised the project, acquired funding, and reviewed/edited the manuscript. All authors reviewed and approved the final manuscript.

Competing interests

The authors declare no competing interests.

Additional information

Supplementary information The online version contains supplementary material available at https://doi.org/10.1038/s41545-025-00470-6.

Correspondence and requests for materials should be addressed to Jing Wang, Guangyang Liu or Donghui Xu.

Reprints and permissions information is available at http://www.nature.com/reprints

Publisher's note Springer Nature remains neutral with regard to jurisdictional claims in published maps and institutional affiliations.

[1]State Key Laboratory of Vegetable Biobreeding, Institute of Vegetables and Flowers, Chinese Academy of Agricultural Sciences, Key Laboratory of Vegetables Quality and Safety Control, Ministry of Agriculture and Rural Affairs of China, Beijing, China. [2]College of Life Sciences, Yantai University, Yantai, China. [3]National Center of Technology Innovation for Comprehensive Utilization of Saline-Alkali Land, Dongying, China. [4]Key Laboratory of Agro-product Quality and Safety, Institute of Quality Standards & Testing Technology for Agro-products, Chinese Academy of Agricultural Sciences, Beijing, China. [5]These authors contributed equally: Dan Xu, Xiaolin Cao, Jie Zhou. ✉e-mail: w_jing2001@126.com; liuguangyang@caas.cn; xudonghui@caas.cn